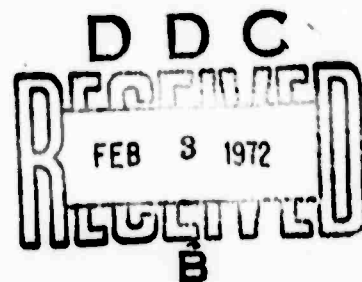# FINAL TECHNICAL SUMMARY REPORT

CONTRACT DAAH01-71-C-1024

DECEMBER 1971

Sponsored by:

ADVANCED RESEARCH PROJECTS AGENCY

ARPA Order No. 360

6837 HAYVENHURST AVENUE, VAN NUYS, CALIF.

xonics, inc.

(213) 787-7380

81

FINAL TECHNICAL SUMMARY REPORT

CONTRACT DAAH01-71-C-1024
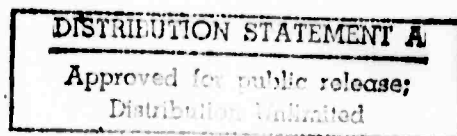
DECEMBER 1971

Sponsored by:

ADVANCED RESEARCH PROJECTS AGENCY
ARPA Order No. 360

XONICS

6837 Hayvenhurst Avenue
Van Nuys, California 91406

TABLE OF CONTENTS

LIST OF ILLUSTRATIONS

SECTION 1.

INTRODUCTION AND SUMMARY

The present technical summary report covers work performed under Contract DAAH01-71-C-1024. The program just completed contained two major tasks. The first was to perform additional data reduction and processing of Lagrangian data on turbulent wakes obtained on a prior contract.[1] In particular, two particle dispersion statistics were sought, to characterize turbulent mixing. The second task was the restoration of the hydrodynamic facility developed under the prior contract and the design of modifications of that facility for use in the study of stratified flows, particularly momentumless wakes.

All tasks were completed during the current program, and the work is described in Sections 2 and 3. The experimental facility and technique, and the data reduction procedures used in obtaining the results discussed here are described in Reference 1, to which the interested reader is referred for background information.

The data processed were obtained from measurements in the wake of a sphere, 4.35 cm in diameter, at a Reynolds number of approximately 1.3×10^5. The most interesting new features evidenced by the additional data analysis are the double structure of the velocity probability distribution, indicating a corresponding double structure of the wake, and the apparent orientation of turbulent eddies at large angles to the wake axis, inferred from angular momentum data. Examination of the two particle separation statistics, while hampered by the relatively small data base, nevertheless provides very interesting results regarding two particle dispersion, particularly, the apparent validity of a local form of Richardson's law of particle dispersion[2] for the turbulent sphere wake, as well as a laminar diffusion behavior of the total particle separation.

The results once more illustrate the wealth of information available in Lagrangian measurements of turbulent flow.

The modified facility has been designed so as to permit simultaneous quantitative observation of both the collapsing wake behind a self propelled body traveling in the stratified tank, and the internal waves and surface currents generated by the wake collapse. The wake stratification mechanism devised was shown capable of producing almost any desired stratification profile simply and efficiently. The optical particle tracker designed

1

for simultaneous tracking of tracer particles in the viewing volume and at the water surface is even simpler than the original scanner, and should allow improved tracking of particles, both in accuracy and field of view.

A brief description of the data reduction procedures used in processing two particle dispersion data is given in Appendix A.

SECTION 2.

TURBULENT WAKE STATISTICS

Lagrangian data have been previously[1] gathered on the turbulent wake of a 4.35 cm diameter towed sphere in water, at a Reynolds number of 1.3×10^5. The data consisted of vector histories of single tracer particles and particle pairs inserted in the wake and tracked by an optical scanner. The bulk of the data reduction and analysis of the single particle data was carried out under a prior contract and has been reported in Reference 1.

Additional data processing and analysis of the single particle data, to further characterize the Lagrangian turbulent velocity field has been carried out under the current contract and is discussed in Section 2.1.

In addition, two particle data, previously not reduced, were reduced and processed to determine two point Lagrangian dispersion statistics, which characterize turbulent mixing. Unfortunately, only a relatively small fraction of the raw data could be successfully processed, due largely to the lapse of approximately one year between the data gathering and reduction. Quite interesting results were obtained nonetheless and are reported in Section 2.2.

2.1 SINGLE PARTICLE STATISTICS

The main emphasis in the additional processing of single particle data during the current program was to further characterize the turbulent velocity field. The previous processing had provided a fairly complete picture of single particle dispersion (i.e., displacement) statistics, and no obvious questions arose that would motivate further analysis. In the present work, some measure of the angular momentum or 'vorticity' statistics in the wake was obtained to characterize more quantitatively the corkscrew motions of fluid tracers observed in the experiments. These are discussed and presented below.

In addition, observation of the experiments indicated that some tracer particles exhibited a distinctly different, far more violent and more 'helical' motion than the bulk of the particles, suggesting a possible 'double' structure of the wake velocity field. These observations motivated examination of the higher moments of the turbulent velocity field, and of the full velocity probability distribution, and those results are also presented and

3

discussed below. As in the case of the single particle data presented in Reference 1, the data have been grouped into three classes, denoted by the subscripts a, b, c, based on initial radial position (i.e., distance from the wake axis). The initial values were, in terms of body diameter D,

$$[r_a(o)/D] \ = \ 0.4 \pm 0.15 \qquad\qquad N_a \ = \ 200$$

$$[r_b(o)/D] \ = \ 0.6 \pm 0.25 \qquad\qquad N_b \ = \ 400$$

$$[r_c(o)/D] \ = \ 1.3 \pm 0.4 \qquad\qquad N_c \ = \ 150$$

the numbers N_a, N_b, N_c indicating the approximate sample size of the specified radial bin.

2.1.1 Angular Momentum Statistics

The distribution of vorticity in a turbulent flow, while theoretically of prime importance in characterizing turbulent eddy structure, is experimentally quite difficult to measure. In a Lagrangian experiment, using tracer particles, vorticity would be measured, strictly speaking, by observing the spin of the tracer particles. While such measurements are in principle feasible, they were not attempted in the experiments under discussion. However, a semiquantitative measure of the eddy structure of the turbulent wake motions can be obtained from the turbulent angular momentum of the tracer particles, defined as

$$\vec{M} \ = \ \vec{r}(t) \times \vec{u}(t) \tag{1}$$

where $\vec{r}(t)$ is the Lagrangian position vector and $\vec{u}(t)$ is the Lagrangian velocity vector. Thus, if the wake turbulence consists of eddies oriented in a particular direction, then the component of $\vec{M}$ in that direction should be large.

More precisely, since the qualitative motion we are seeking to characterize is a helicoidal motion about some mean trajectory, as illustrated schematically below,

4
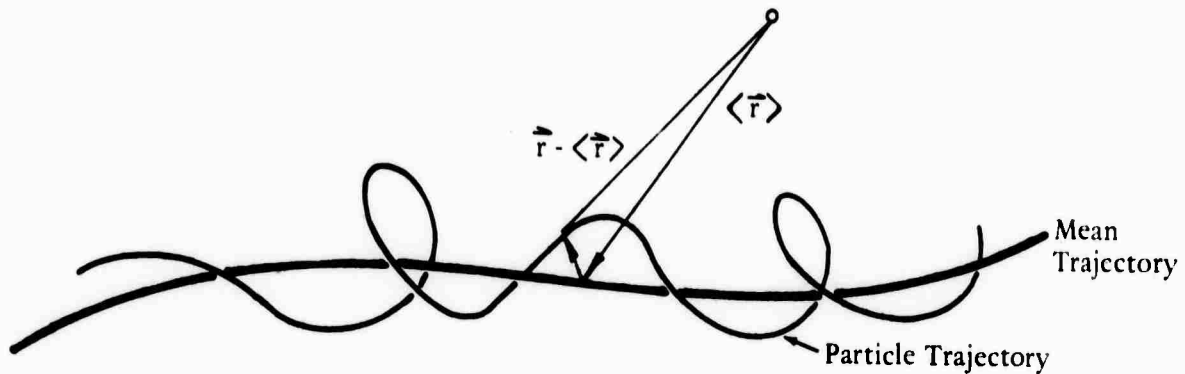
the quantities actually computed were the mean square components of the vector

$$\vec{L}(t) = \left\{ \vec{r}(t) - \langle \vec{r}(t) \rangle \right\} \times \left\{ \vec{V}(t) - \langle \vec{V}(t) \rangle \right\} \tag{2}$$

The results are shown in Figures 1a, 1b, and 1c for the components $\langle L_z^2 \rangle$ and $\langle L_T^2 \rangle$ = ½ $\left\{ \langle L_y^2 \rangle + \langle L_x^2 \rangle \right\}$, z being the axial direction, y the vertical and x the other (horizontal) transverse direction.

As in the previous data, lengths are in units of body diameter and velocities in units of body velocity, so that L^2 is in units of $V_\infty^2 D^2$.

The wake axisymmetry is again visible in the comparison between $\langle L_y^2 \rangle$ and $\langle L_x^2 \rangle$ shown in Figure 2, as it was in comparisons between the two transverse components $\langle v^2 \rangle$ and $\langle w^2 \rangle$.

As in the case of the turbulent velocity decay, the angular momentum decay curves can be fitted reasonably well with power law (straight line) fits. The results of least squares fits are given below for each component and each radial 'bin'.
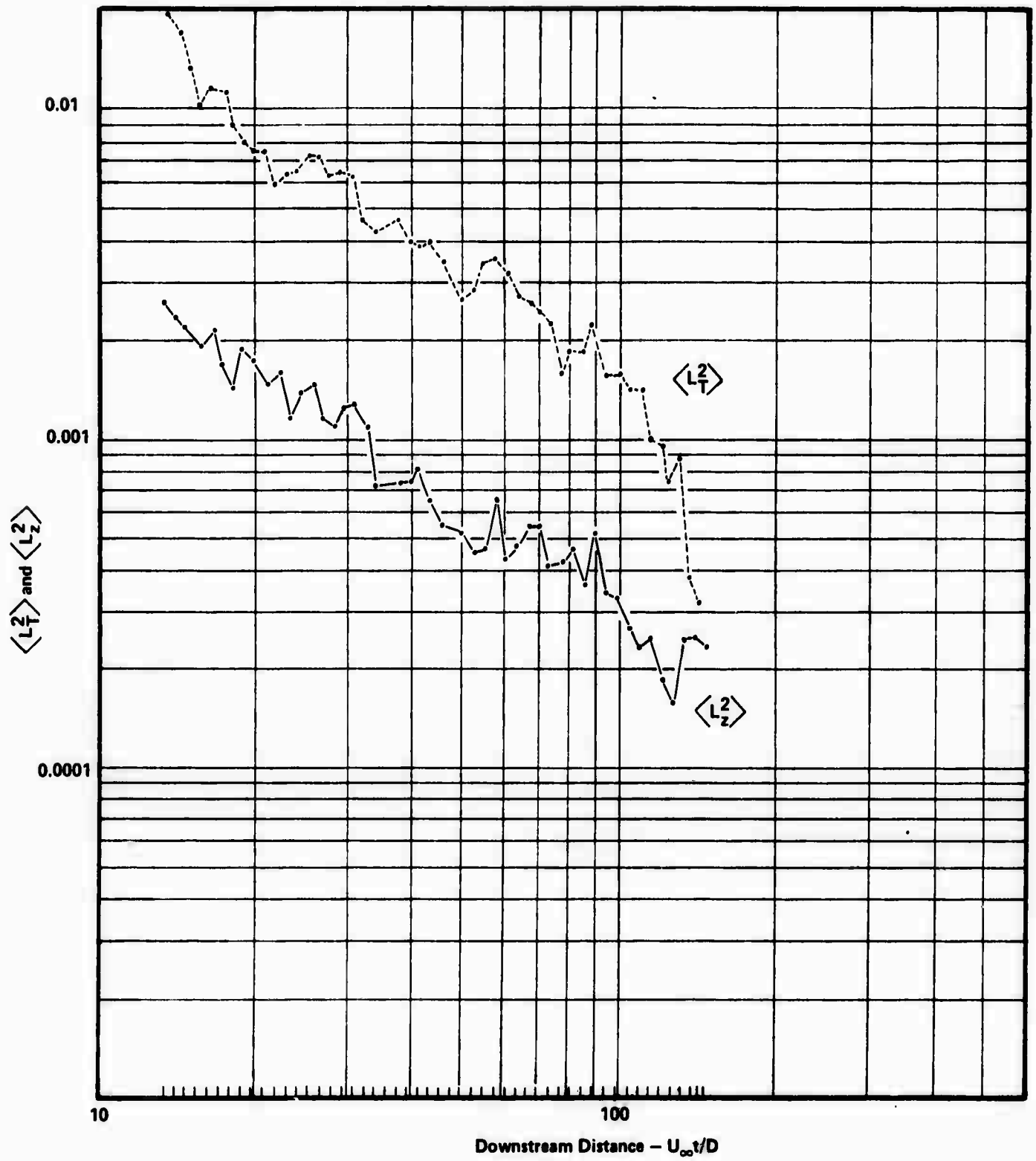
Figure 1a. Axial and Transverse Mean Square Angular Momentum Core Data.
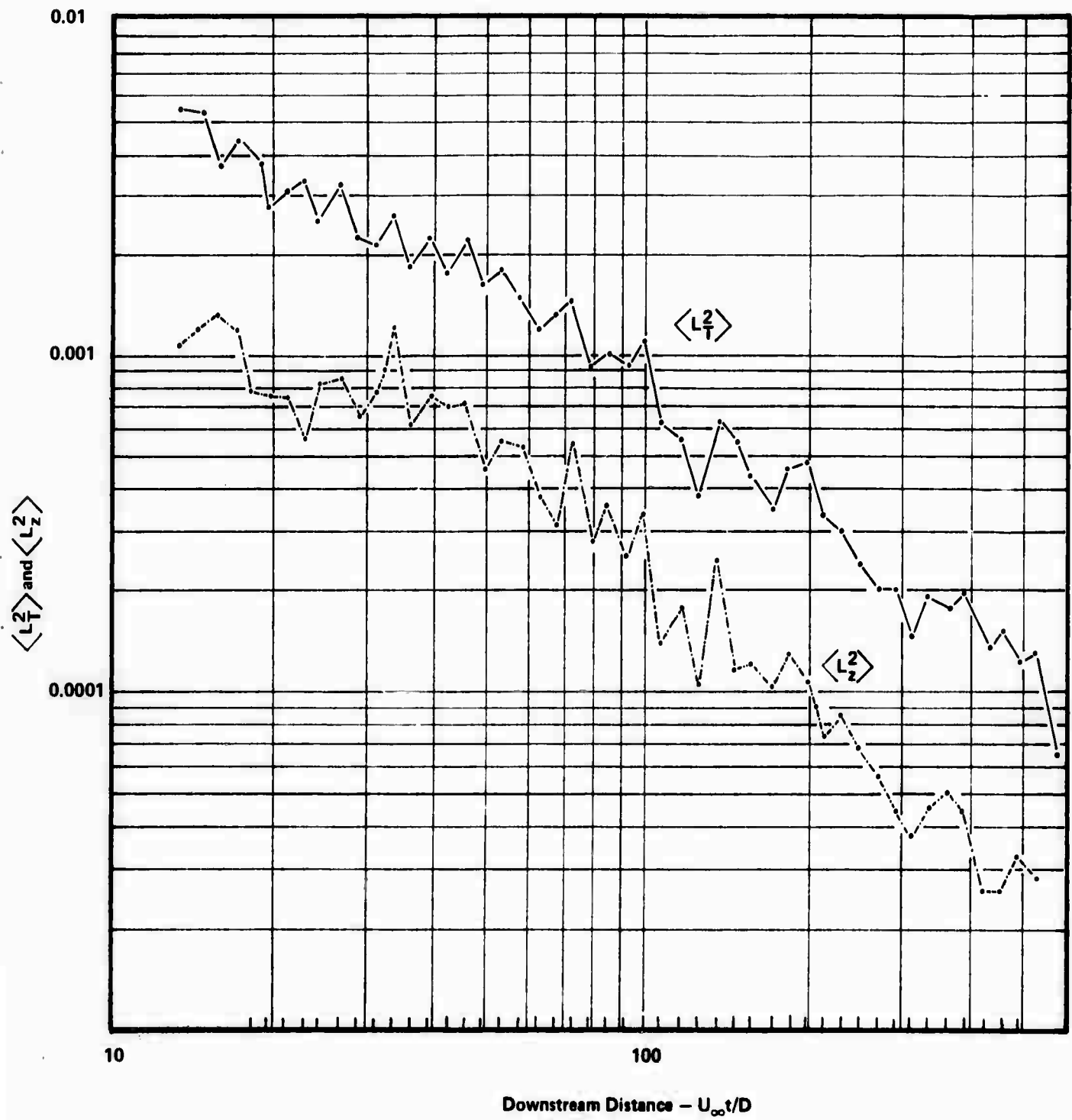
Figure 1b. Axial and Transverse Mean Square Angular Momentum Inner Data.
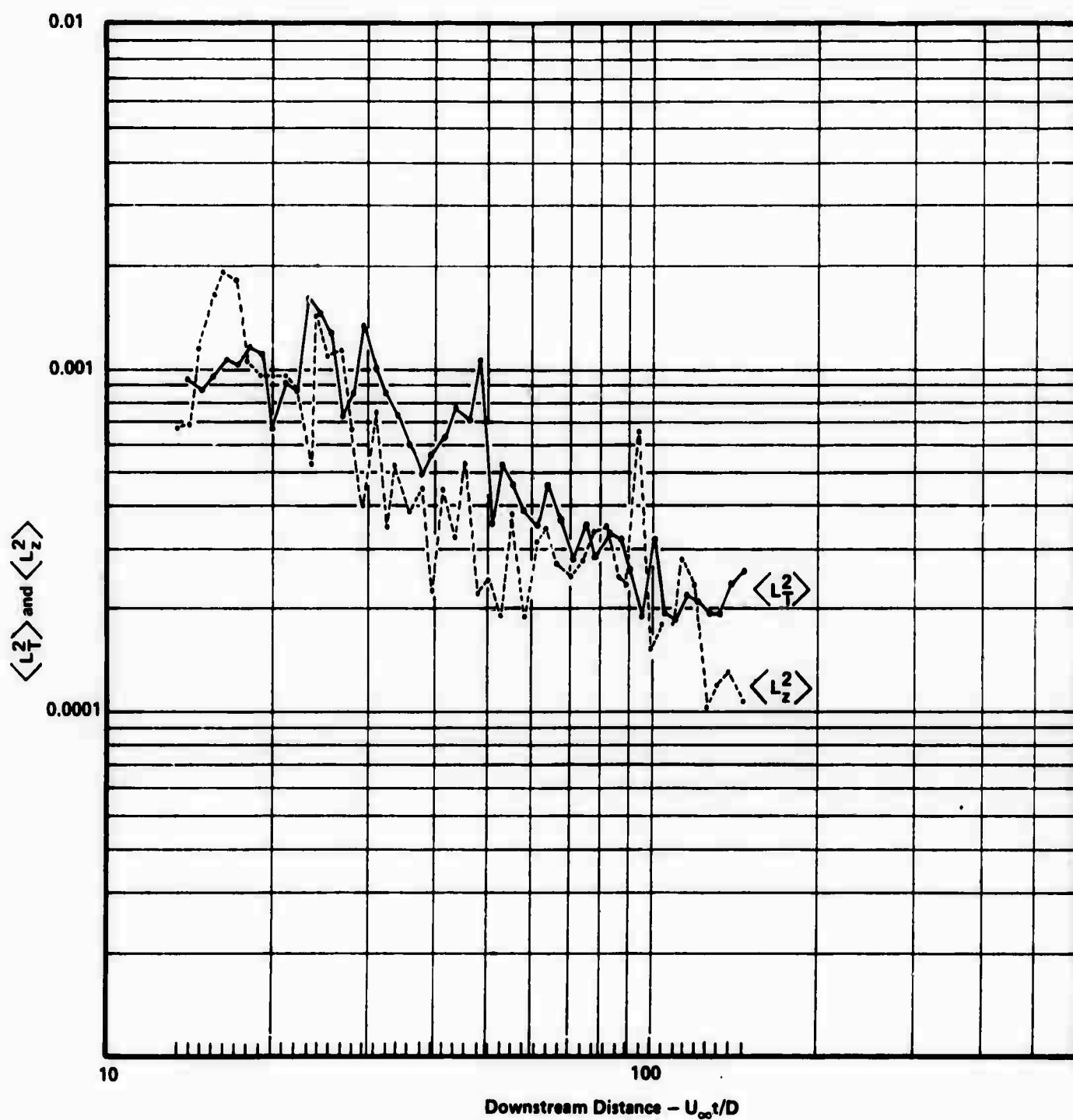
Figure 1c. Axial and Transverse Mean Square Angular Momentum Outer Data.

8
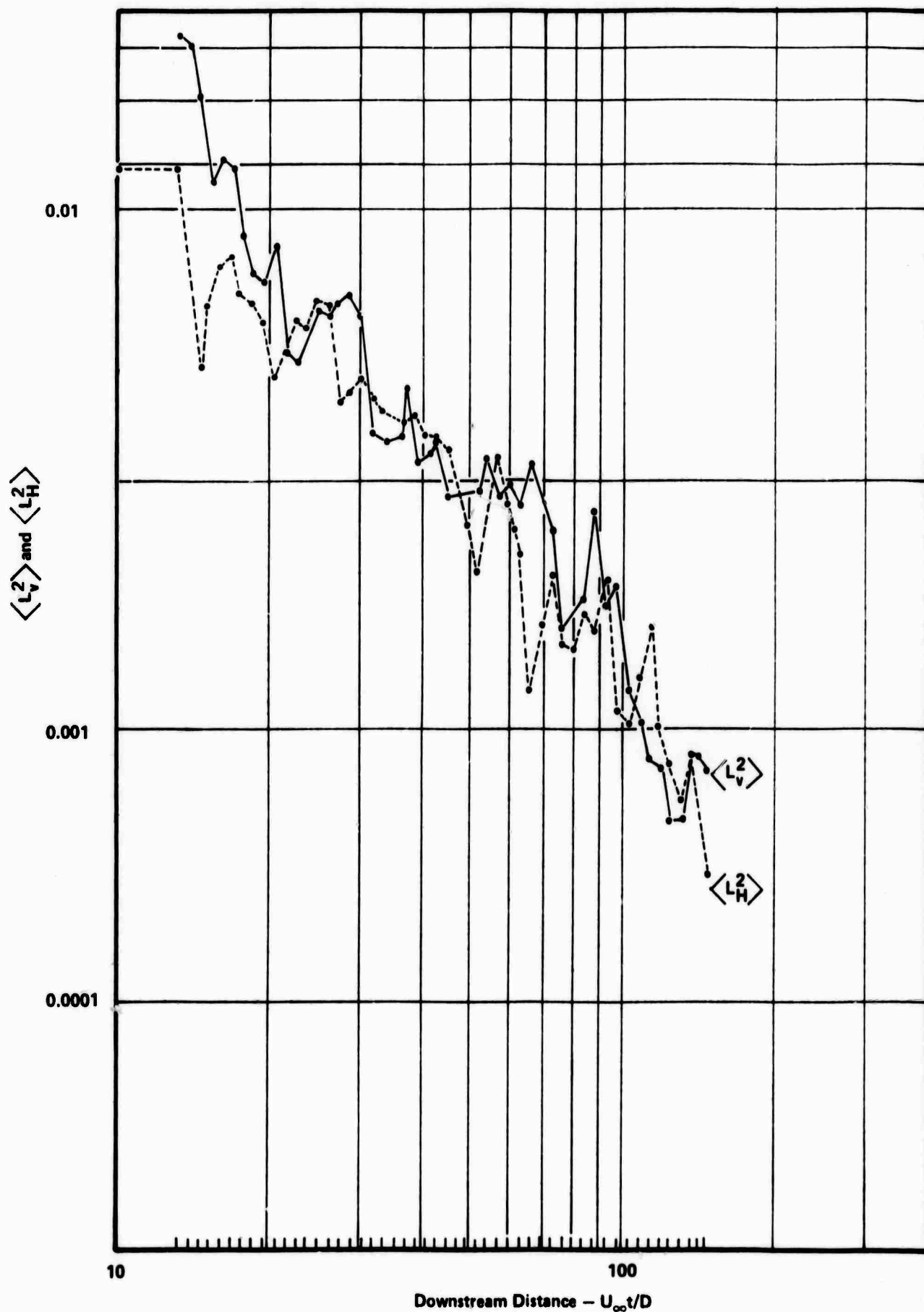
Figure 2. Vertical and Horizontal Mean Square Angular Momentum Core Data.

Core Data:

$$\langle L_z^2 \rangle = 0.028 \, \zeta^{-0.98}$$

$$\tfrac{1}{2} \langle L_x^2 + L_y^2 \rangle = 0.30 \, \zeta^{-1.17}$$

(3a)

Inner Wake Data:

$$\langle L_z^2 \rangle = 0.044 \, \zeta^{-1.16}$$

$$\tfrac{1}{2} \langle L_x^2 + L_y^2 \rangle = 0.076 \, \zeta^{-1.0}$$

(3b)

Outer Wake Data:

$$\langle L_z^2 \rangle = 0.023 \, \zeta^{-1.07}$$

$$\tfrac{1}{2} \langle L_x^2 + L_y^2 \rangle = 0.012 \, \zeta^{-0.83}$$

(3c)

It is worthwhile to note that the slopes for $\langle L_z^2 \rangle$ and $\langle L_T^2 \rangle$ decay are substantially less than those for the turbulent velocities. This is not surprising, since the 'moment arm' factor in the angular momentum, i.e., the (single particle) dispersion, is increasing with downstream distance. However, it may also be noted that quantities such as $\langle u^2 \rangle \langle (x-x_o)^2 \rangle$ or $\langle v^2 \rangle \langle (y-y_o)^2 \rangle$ decay still more slowly than $\langle L^2 \rangle$, so that the 'normalized vorticity' of the velocity fluctuations is actually decreasing with downstream distance, (i.e., with respect to the turbulence intensity), indicating a decay of the effective Reynolds number of the turbulence. Two other noteworthy characteristics of the mean square turbulent angular momentum are evident in the results shown in Figures 1 and 2.

First, it is clear that the axial mean square angular momentum,

$$\langle L_z^2 \rangle = \left\langle \left\{ (x - \bar{x})(v - \bar{v}) - (y - \bar{y})(w - \bar{w}) \right\}^2 \right\rangle$$

(4)

is considerably smaller than the transverse angular momentum

10

$$\langle L_T^2\rangle \equiv \tfrac{1}{2}\langle L_x^2\rangle + \tfrac{1}{2}\langle L_y^2\rangle = \tfrac{1}{2}\langle\{(z-\overline{z})(v-\overline{v})-(y-\overline{y})(u-\overline{u})\}^2\rangle$$
$$+ \tfrac{1}{2}\langle\{(z-\overline{z})(w-\overline{w})-(x-\overline{x})(u-\overline{u})\}^2\rangle, \tag{5}$$

for the core and inner wake data.

On the other hand, the mean square axial and transverse turbulent velocities, $\langle u^2\rangle$ and $\tfrac{1}{2}\langle v^2+w^2\rangle$, as may be seen from the power law fits in Eqs. (6) and (7) below, taken from Reference 1, can be seen to be approximately equal. In fact, if anything $\langle u^2\rangle$ is somewhat larger than $\tfrac{1}{2}\langle v^2+w^2\rangle$, so that the differences in the turbulent mean square angular momentum components are not due to any differences in turbulent velocity fluctuation components.

We therefore conclude that the turbulent eddies in the wake of a sphere are oriented with their axes almost orthogonal to the direction of mass flow. The same feature has been noted of course by Townsend[3] in his studies of the turbulent wake behind a cylinder. Again, however, one should be cautioned against too close a quantitative comparison between Eulerian and Lagrangian sphere wake measurements.

From the measured ratio of axial to transverse mean square angular momentum of approximately 0.25 to 0.3, we may infer that the eddies are oriented at an angle

$$\theta \simeq \cos^{-1}\frac{\langle L_z^2\rangle}{\langle L_z^2\rangle + \langle L_x^2\rangle + \langle L_y^2\rangle} \simeq 75° - 80°$$

with respect to the wake axis.

The second clear feature of the turbulent angular momentum results is the low value for all components of the angular momentum in the outer wake, compared to the core and inner wake values. The corresponding velocity values for the outer wake, while definitely lower than those for the core and inner wake, are not in the same ratio as the angular momenta. Thus, for example, the transverse mean square velocities in the core and outer wakes can be fitted approximately by the power law fits

$$\langle v^2 + w^2 \rangle \simeq 3.2 \times 10^{-1} \zeta^{-1.54} \qquad \text{Core}$$

$$(6)$$

$$\langle v^2 + w^2 \rangle \simeq 4 \times 10^{-2} \zeta^{-1.2} \qquad \text{Outer Wake}$$

where ζ is downstream distance measured in body diameters. The corresponding fits for the mean square velocities are

$$\langle u^2 \rangle \simeq 2.8 \times 10^{-1} \zeta^{-1.6} \qquad \text{Core}$$

$$(7)$$

$$\langle u^2 \rangle \simeq 4 \times 10^{-2} \zeta^{-1.28} \qquad \text{Outer Wake}$$

Thus, for example, if we were to 'renormalize' the transverse angular momenta, as fitted by the power law expression in Eqs. (3), by dividing them through by the corresponding transverse or axial mean square velocities, then take the ratio of 'renormalized' angular momenta for the core and outer wakes, we would find

$$\frac{\left[\langle L_T^2 \rangle / \langle u^2 \rangle \right]_{\text{outer}}}{\left[\langle L_T^2 \rangle / \langle u^2 \rangle \right]_{\text{core}}} \simeq 0.27$$

for all values of downstream distance.

The inference from the above result, remembering that angular momentum may be considered as an index of vorticity, is that the turbulent velocity fluctuations in the outer wake are not connected with a significant eddy structure, and that the vorticity fluctuations in the outer wake region are very low. Classically, the turbulent core is distinguished from the region of potential flow outside it by the presence of vorticity fluctuations, which are absent in the external region in spite of significant velocity fluctuations. The present result again confirms, as have most of our previous results, the 'classical' picture of the structure of the incompressible wake developed through Eulerian measurements, but again, we must caution against too direct a comparison between the two sets of experimental results.

12

2.1.2 Velocity Probability Distribution

In Reference 1, the mean and mean square fluctuations of the Lagrangian veloci- ties, as a function of time or downstream distance, were presented. It was pointed out in that report that a complete picture of the fluid particle velocities could not be obtained by the first two velocity moments. For that reason, the third and fourth order moments of the velocity were also obtained, and indicated that the velocity probability distribution was both skewed and had a large flatness factor.

On the other hand, visual observations of fluid particle motions suggested a possible double structure to the fluid particle motions, in which, to the dominant 'normal' turbulent motions were added, occasionally, some very energetic motions, mostly in the form of very tight spiral motions. These higher velocity motions were definitely not associated with entrainment in a recirculation region, and often would not occur until a few seconds after passage of the body.

In view of the statistical and visual evidence of a non-simple velocity probability distribution, it appeared that velocity probability histograms would be worth generating, in spite of a rather small data base for such purposes. The results are shown in Figures 3 through 8, for the core, inner wake and outer wake particles, and at three values of time after passage of the body, expressed in downstream distance.

The three values of downstream distance are 13.3, 57.3 and 246 body diameters. Note that the velocity scale used in the histograms is not uniform: in order to avoid collapse of the late time distributions into the center, the unit of velocity used in each scale is the standard deviation of the velocity distribution, for the core particles, at the measurement time. (Thus, the outer wake scale is not the standard deviation of the outer wake velocities.) A double structure of the histograms representing the axial and transverse velocity distributions of the center or core wake particles is definitely discernible, and more particularly for the early time axial velocity distribution. The transverse velocity histogram shows a less distinct secondary peak.

The inner wake particles do not exhibit noticeable secondary peaks in the velocity histograms for either the axial or the vertical component. Furthermore, while the axial distributions are definitely skewed, the transverse distributions are in fact rather symmetric. The outer wake distribution also fails to exhibit a double structure.

13

Figure 3a. Axial Velocity Probability Histograms Core Data. Wake Position = 13.3 BD.

NORMALIZED VELOCITY

Figure 3b. Axial Velocity Probability Histograms Core Data. Wake Position = 57.3 BD.

NORMALIZED VELOCITY

Figure 3c. Axial Velocity Probability Histograms Core Data. Wake Position = 246 BD.

Figure 4a. Axial Velocity Probability Histograms Inner Data. Wake Position = 13.3 BD.

Figure 4b. Axial Velocity Probability Histograms Inner Data. Wake Position = 57.3 BD.

18

Figure 4c. Axial Velocity Probability Histograms Inner Data. Wake Position = 246 BD.

Figure 5a. Axial Velocity Probability Histogram Outer Data.
Wake Position = 13.3 BD.

Figure 5b. Axial Velocity Probability Histogram Outer Data.
Wake Position = 57.3 BD.

21

Figure 5c. Axial Velocity Probability Histogram Outer Data.
Wake Position = 246 BD.

Figure 6a. Transverse Velocity Probability Histogram Core Data. Wake Position = 13.3 BD.

Figure 6b. Transverse Velocity Probability Histogram Core Data. Wake Position = 53.7 BD.

24

Figure 6c. Transverse Velocity Probability Histogram Core Data. Wake Position = 246 BD.

Figure 7a. Transverse Velocity Probability Histogram Inner Data. Wake Position = 13.7 BD.
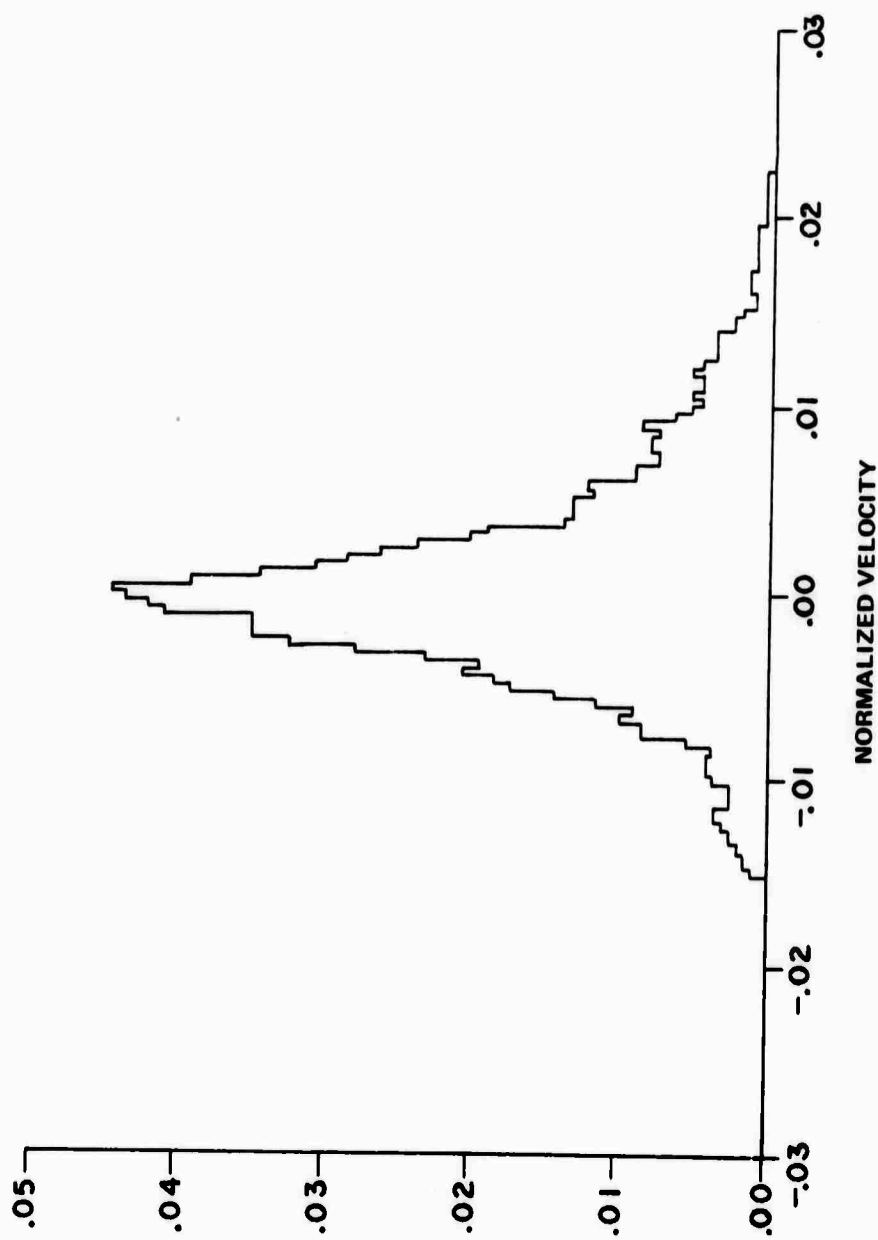
Figure 7b. Transverse Velocity Probability Histogram Inner Data. Wake Position = 57.3 BD.
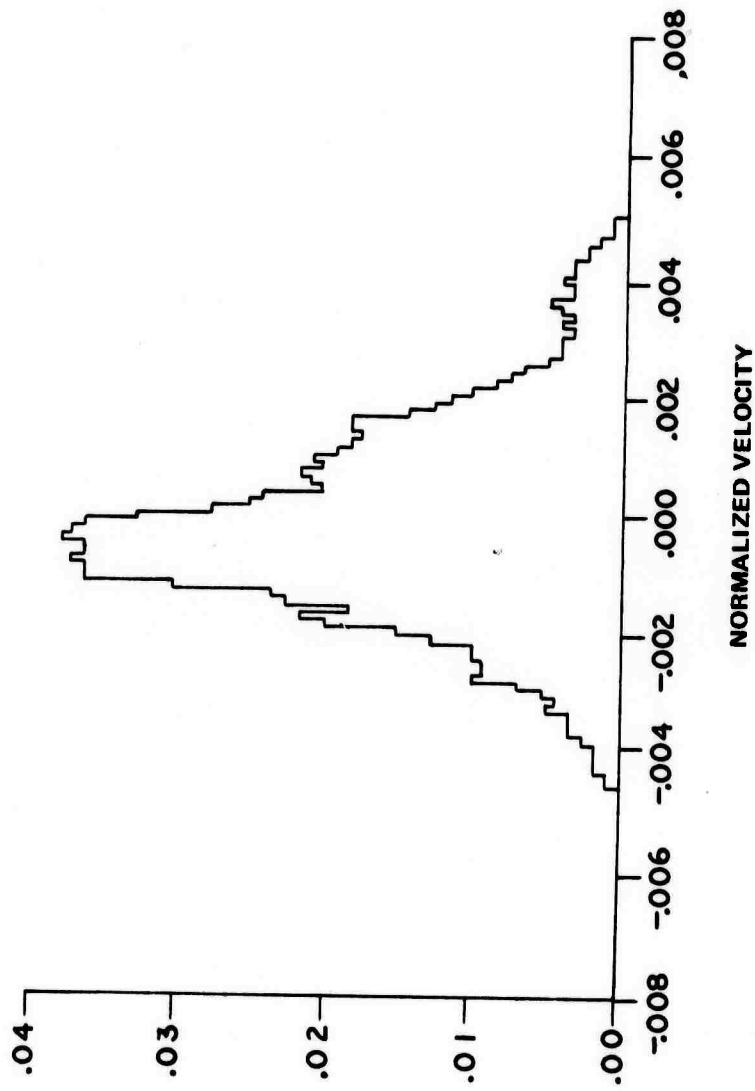
Figure 7c. Transverse Velocity Probability Histogram Inner Data. Wake Position = 246 BD.
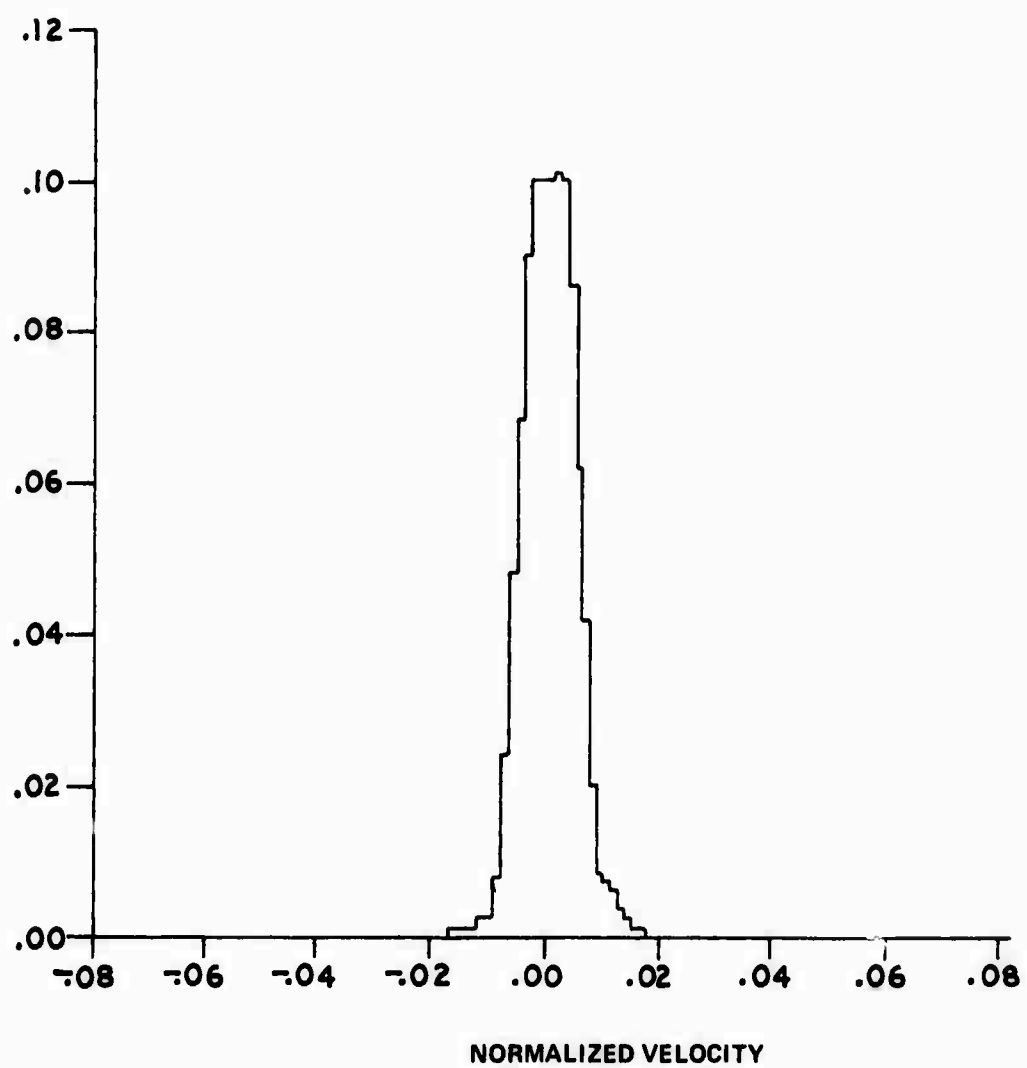
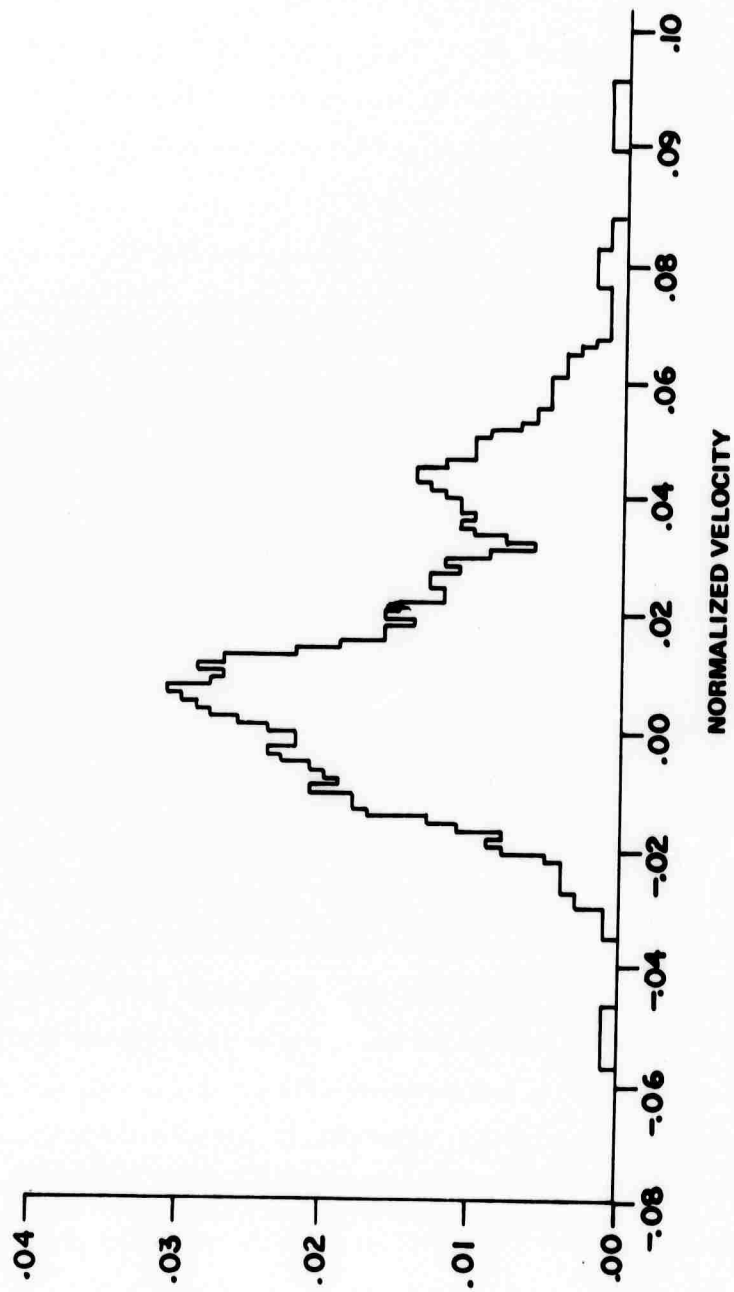Figure 8a. Transverse Velocity Probability Histogram Outer Data.
Wake Position = 13.3 BD.
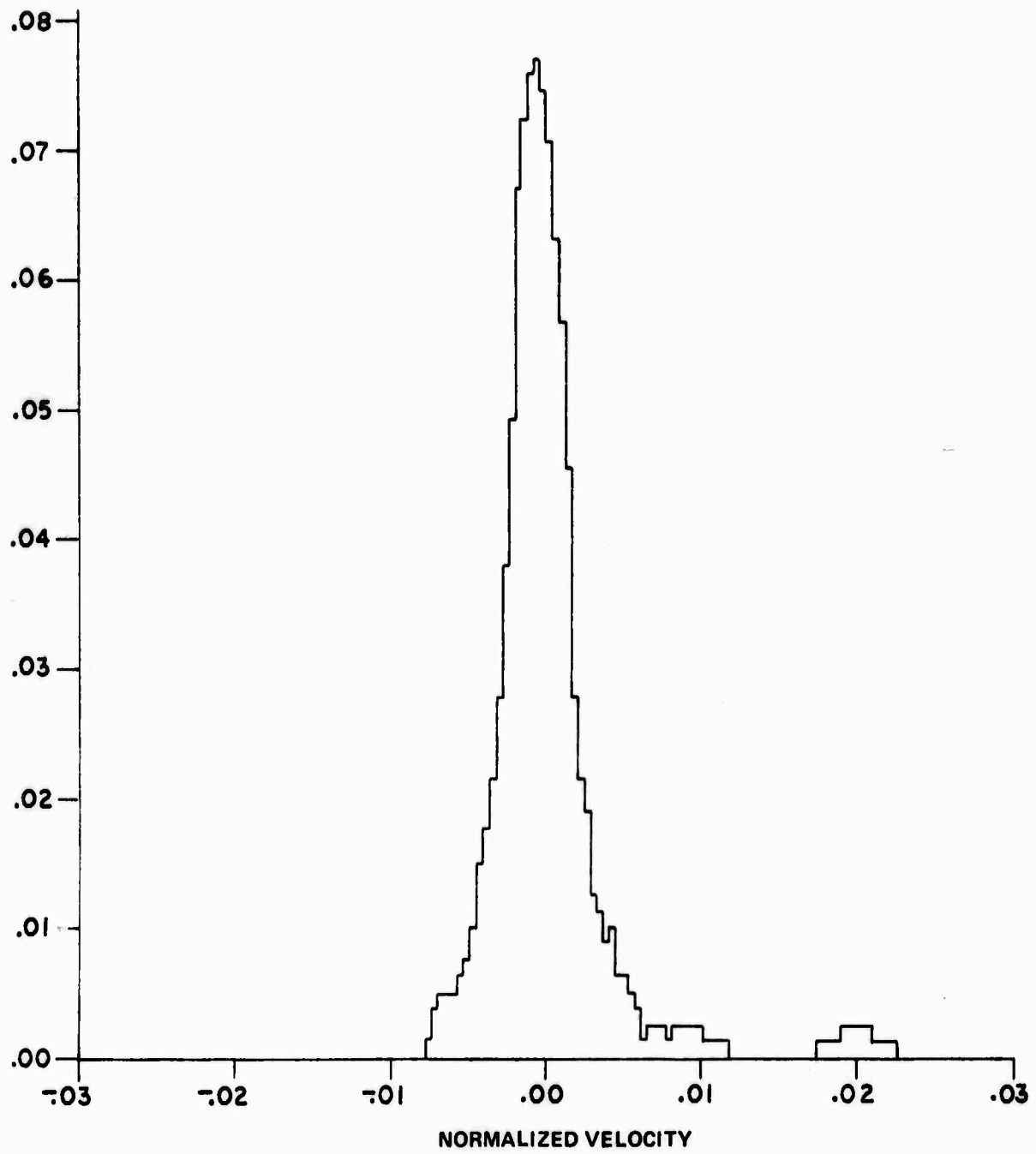
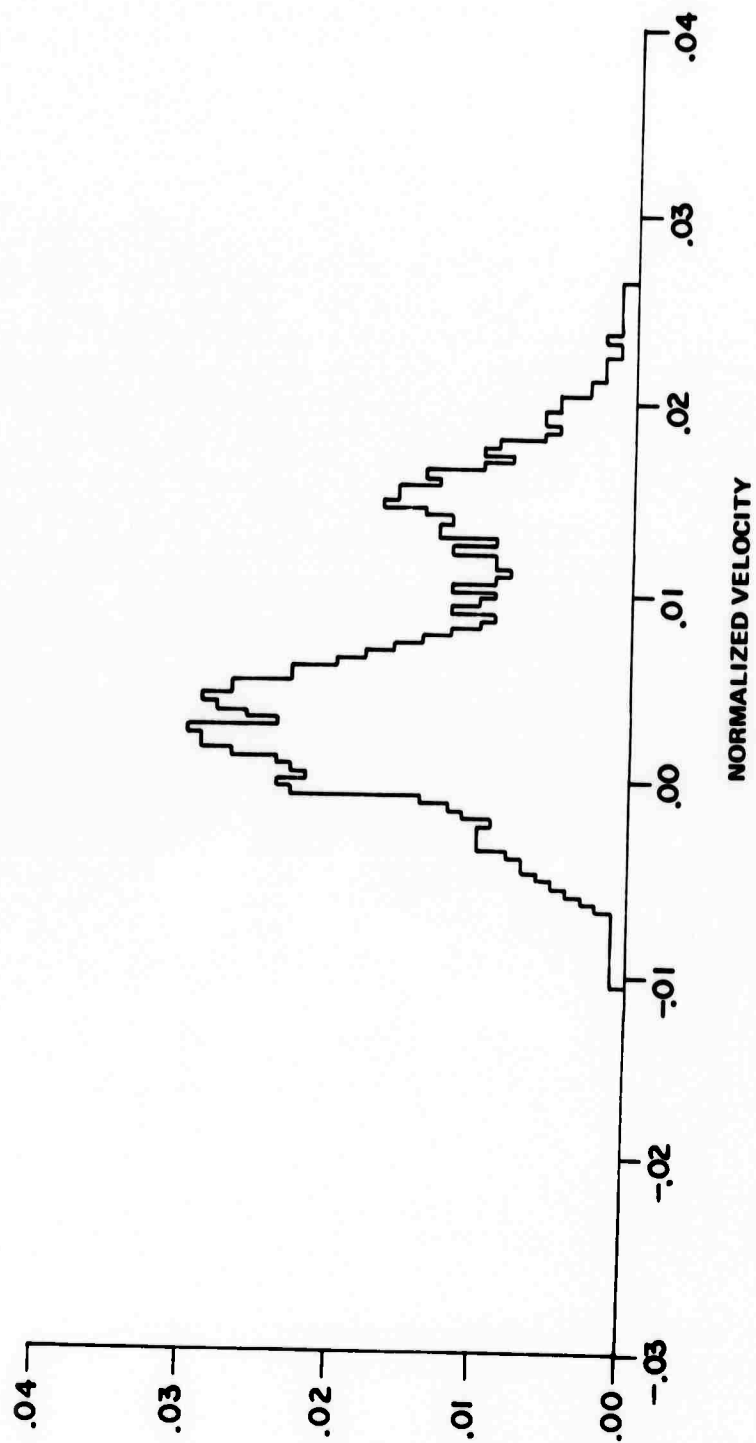Figure 8b. Transverse Velocity Probability Histogram Outer Data.
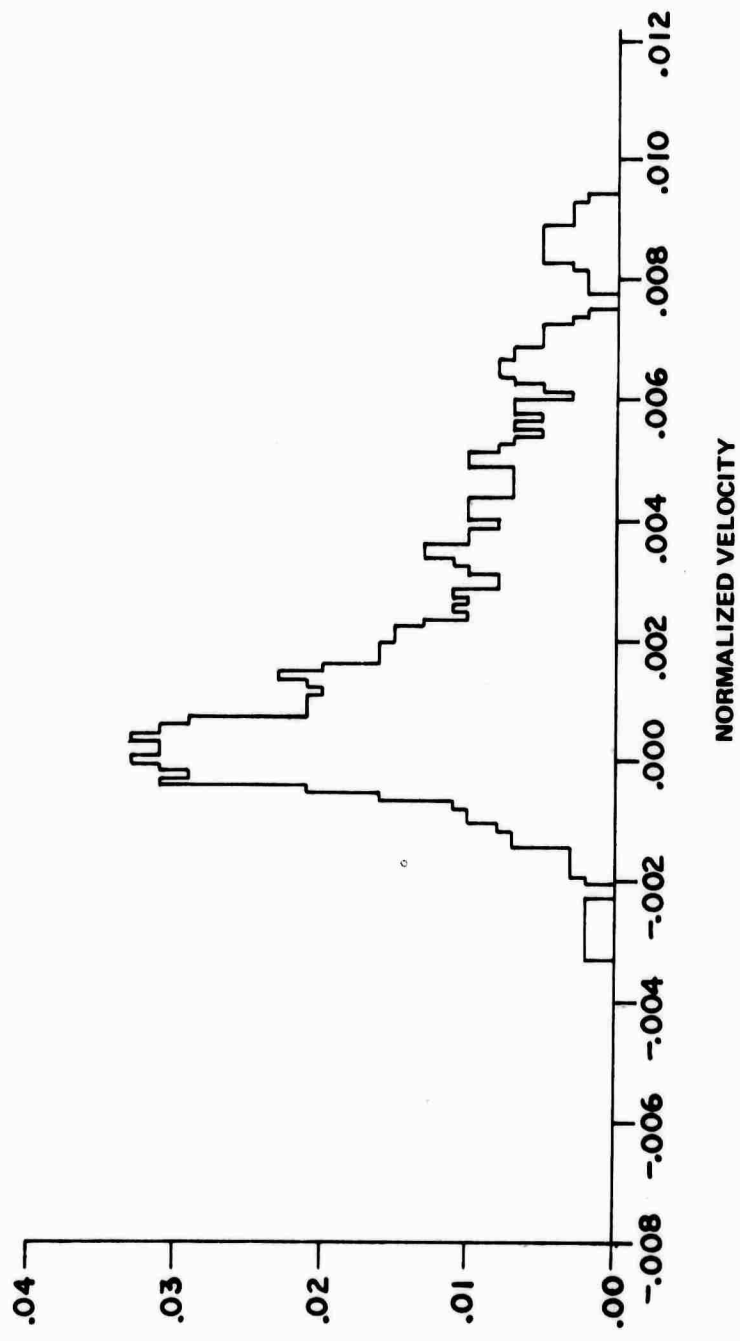Wake Position = 57.3 BD.
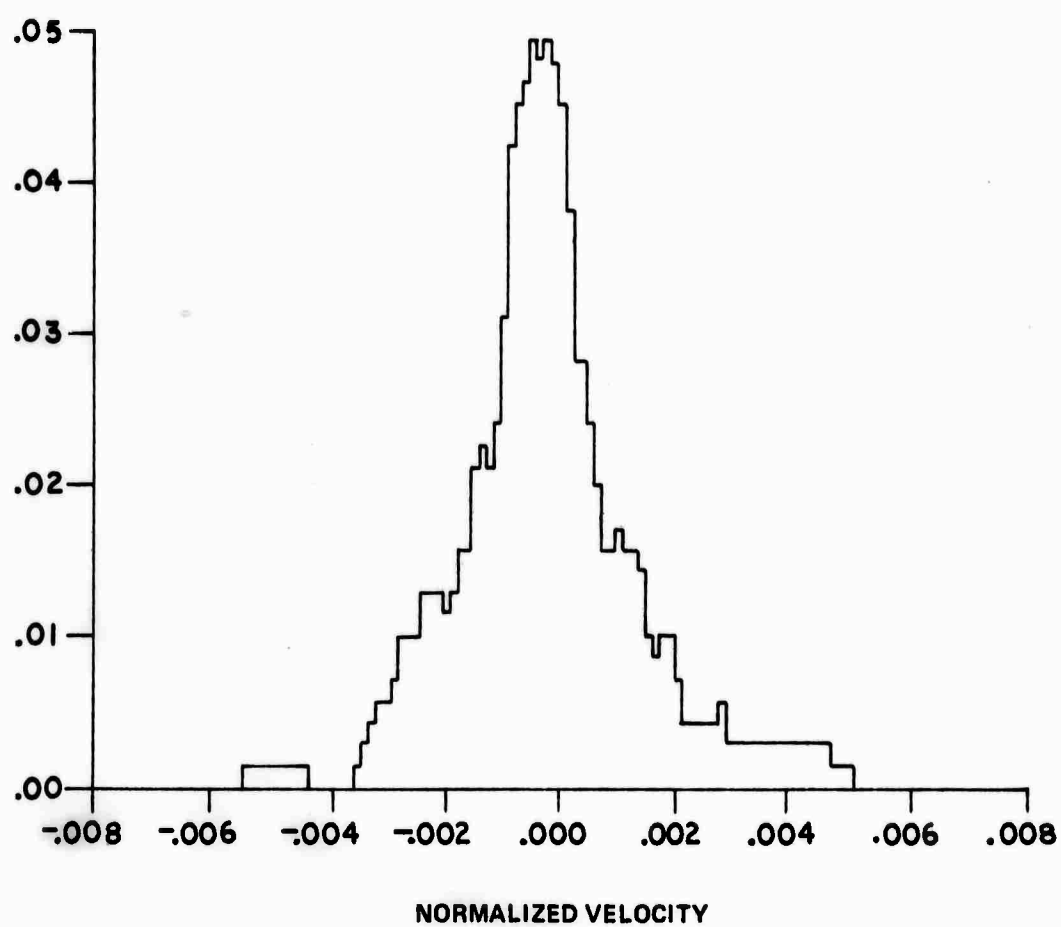
Figure 8c. Transverse Velocity Probability Histogram Outer Data.
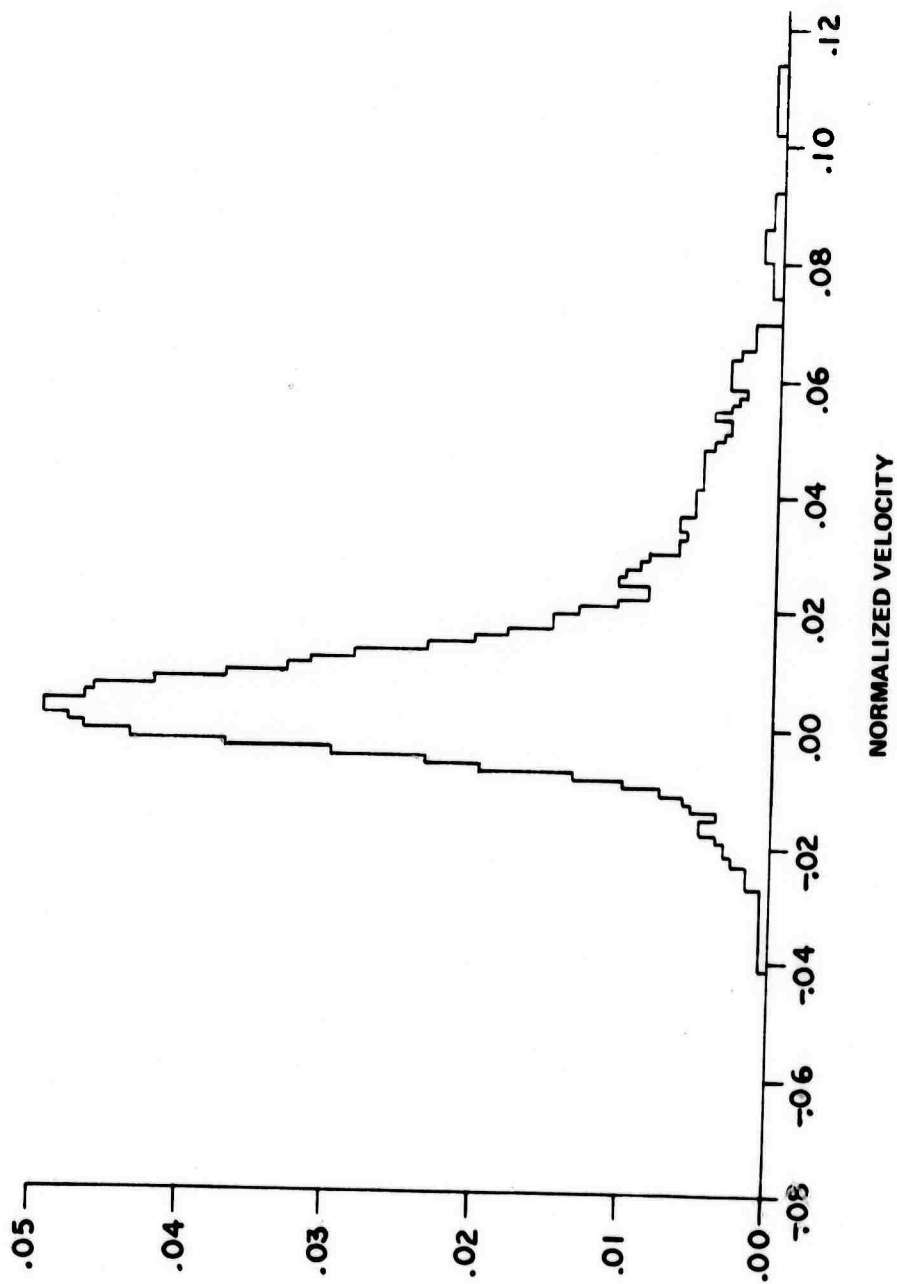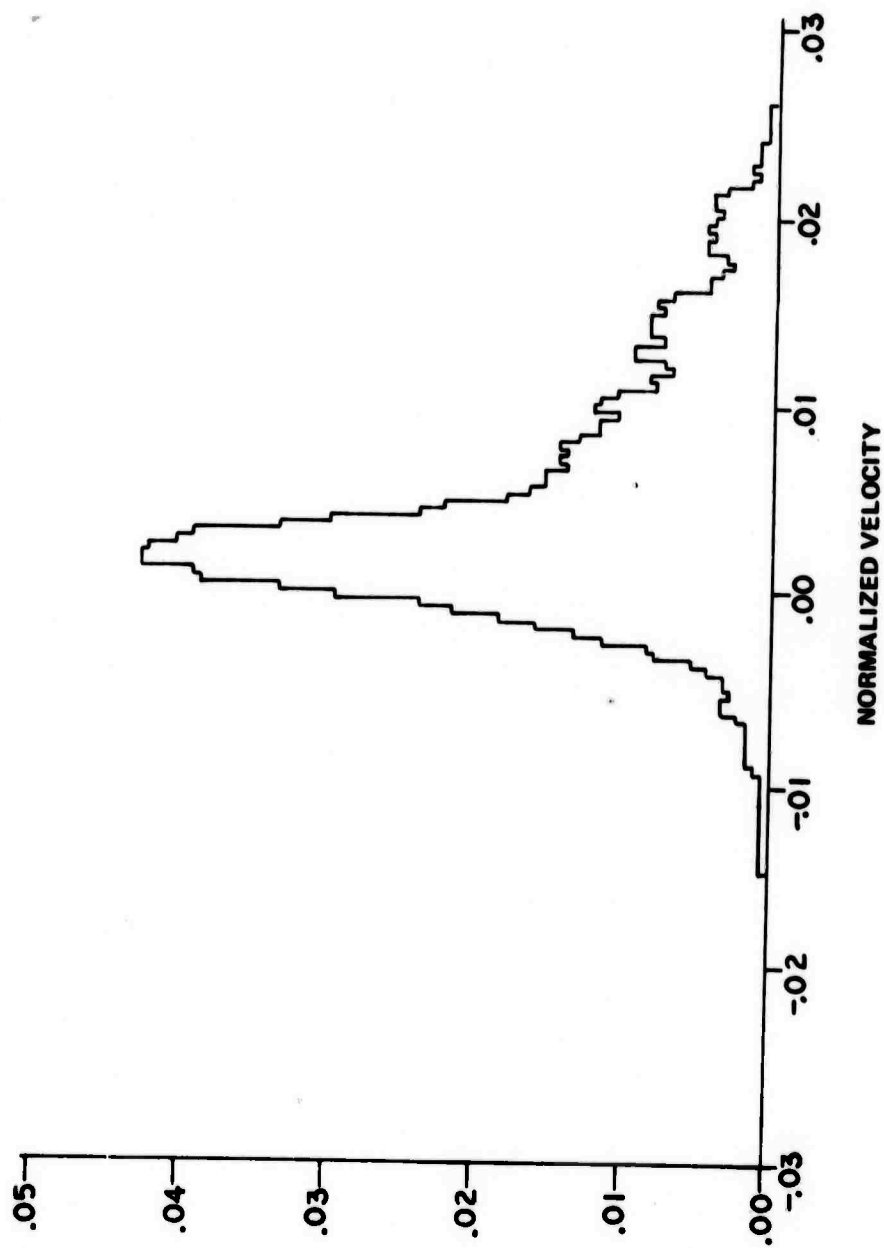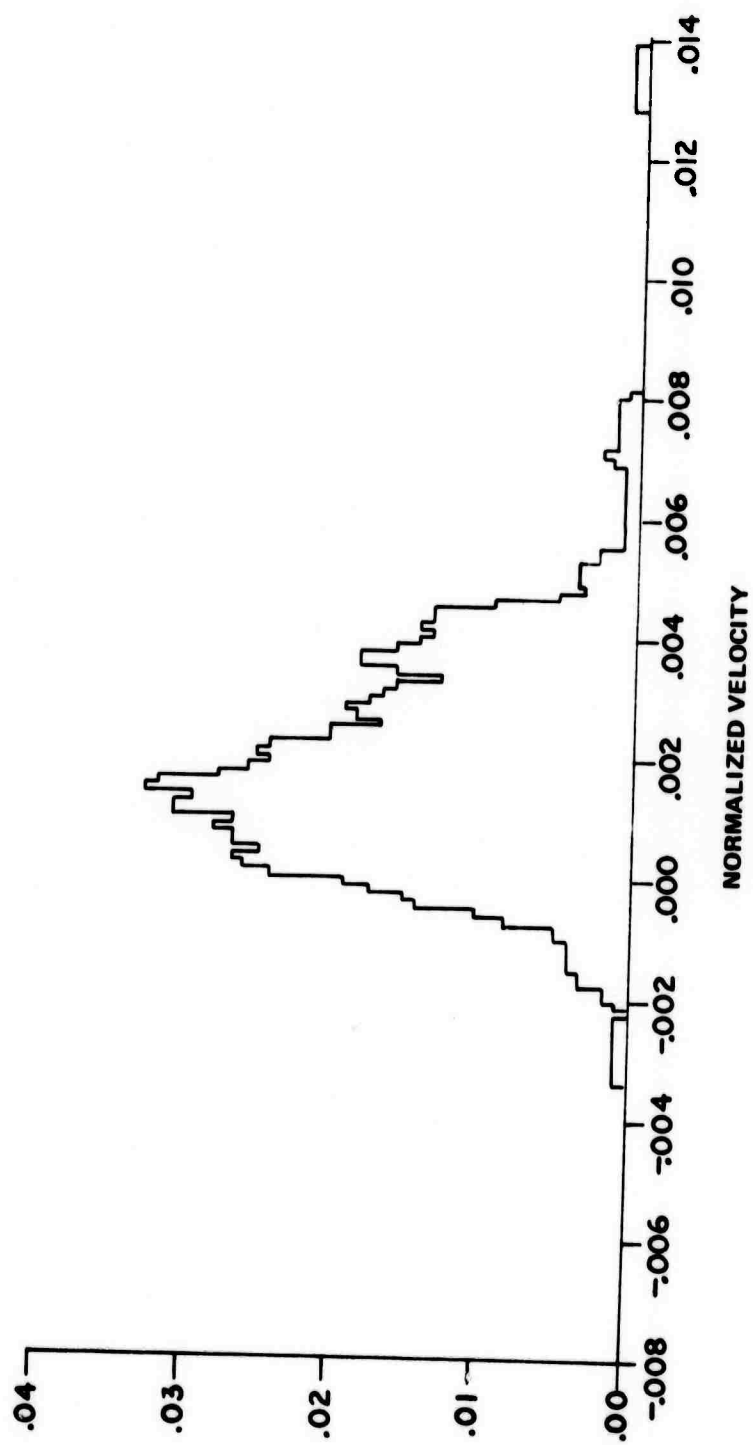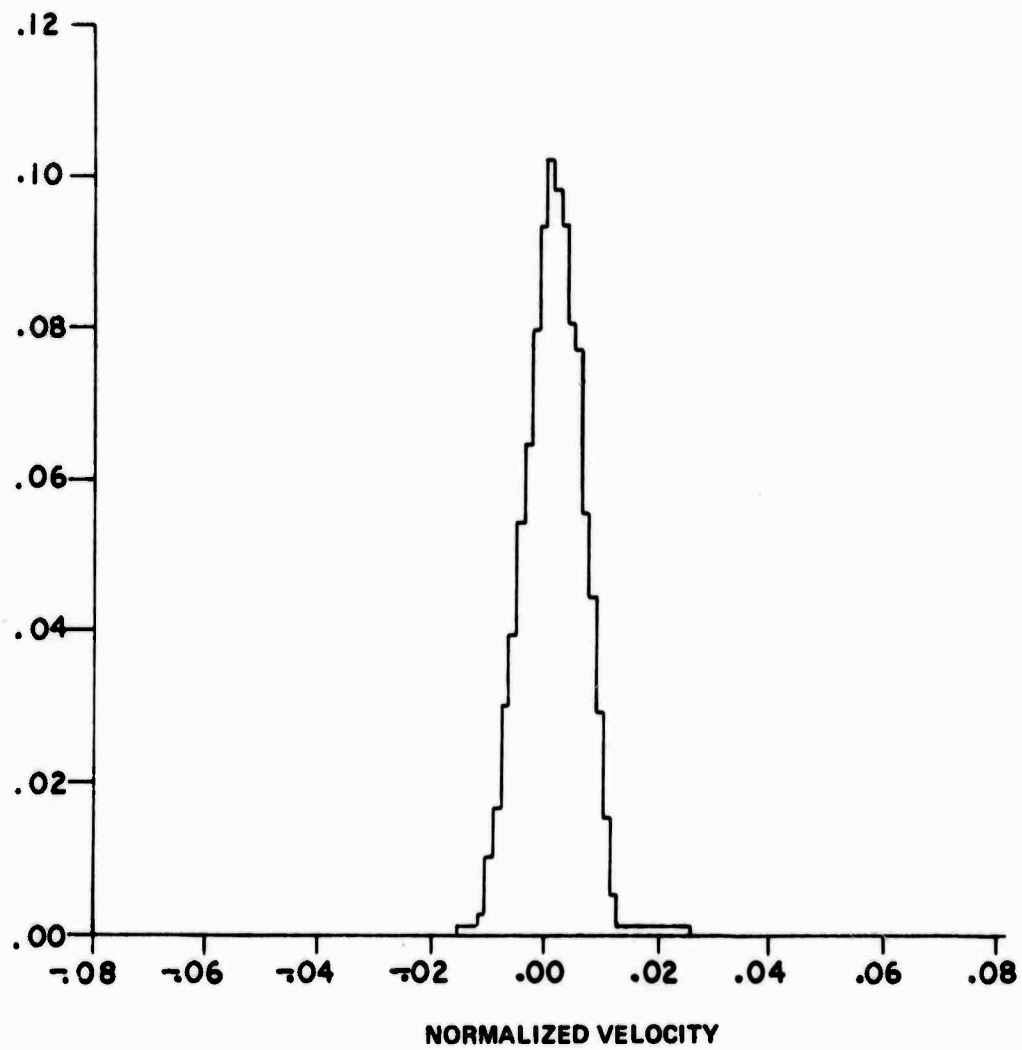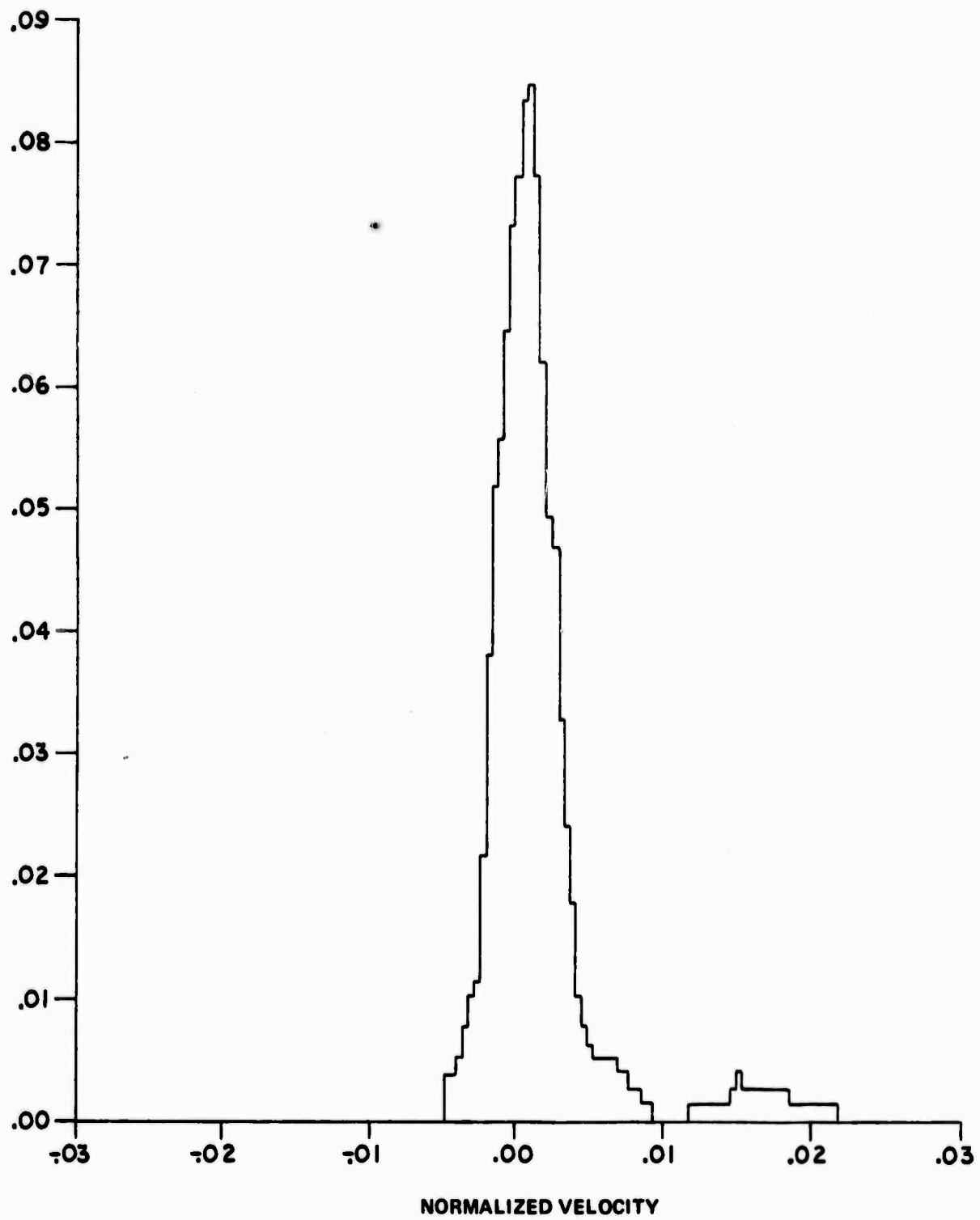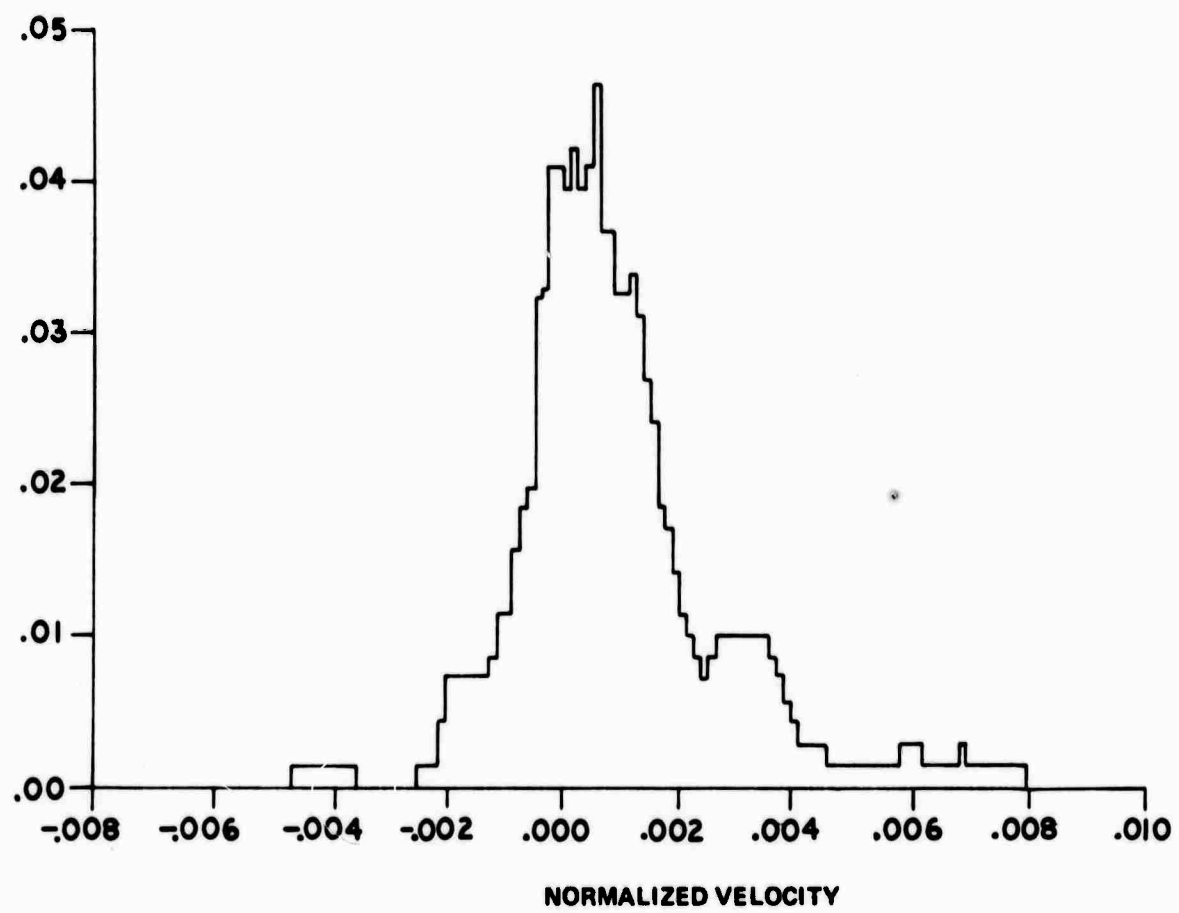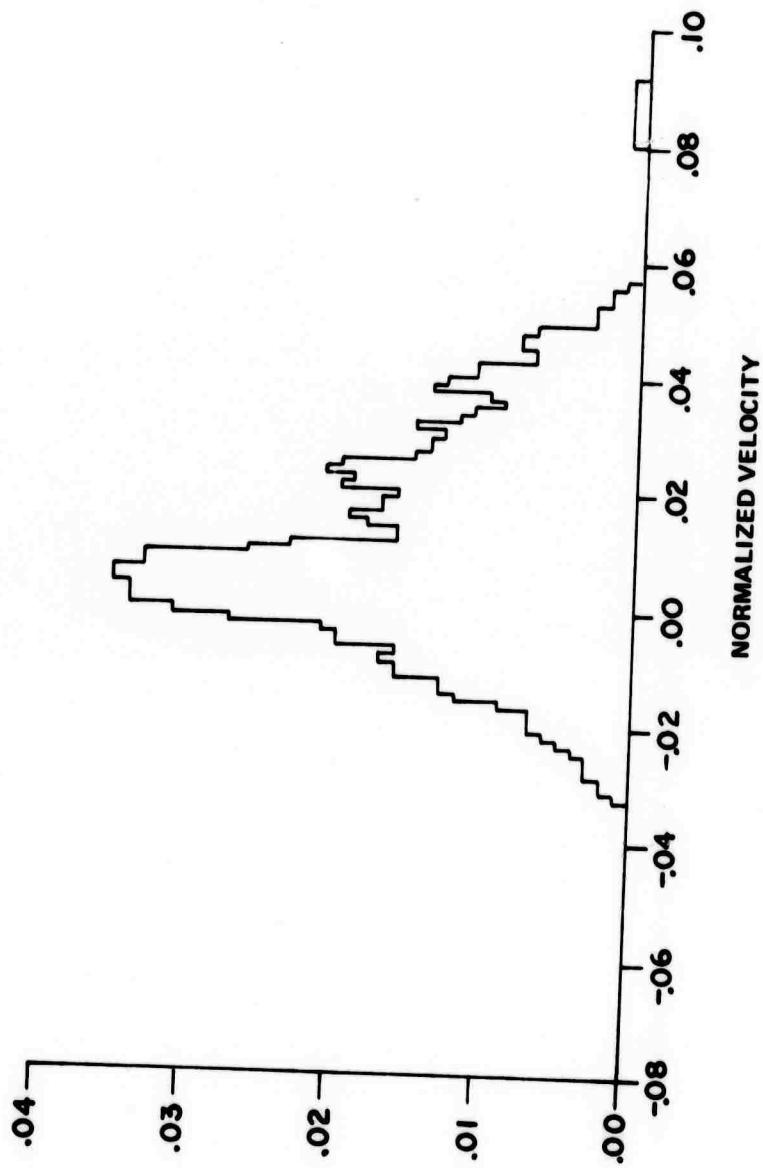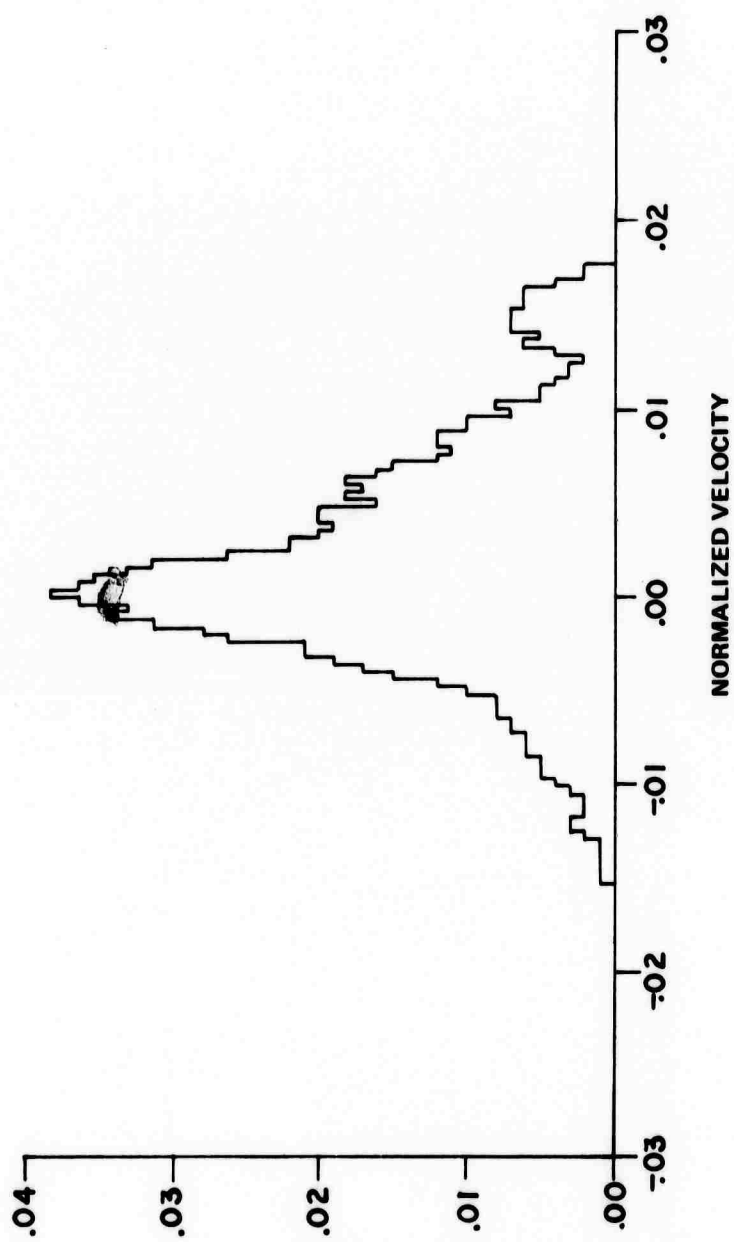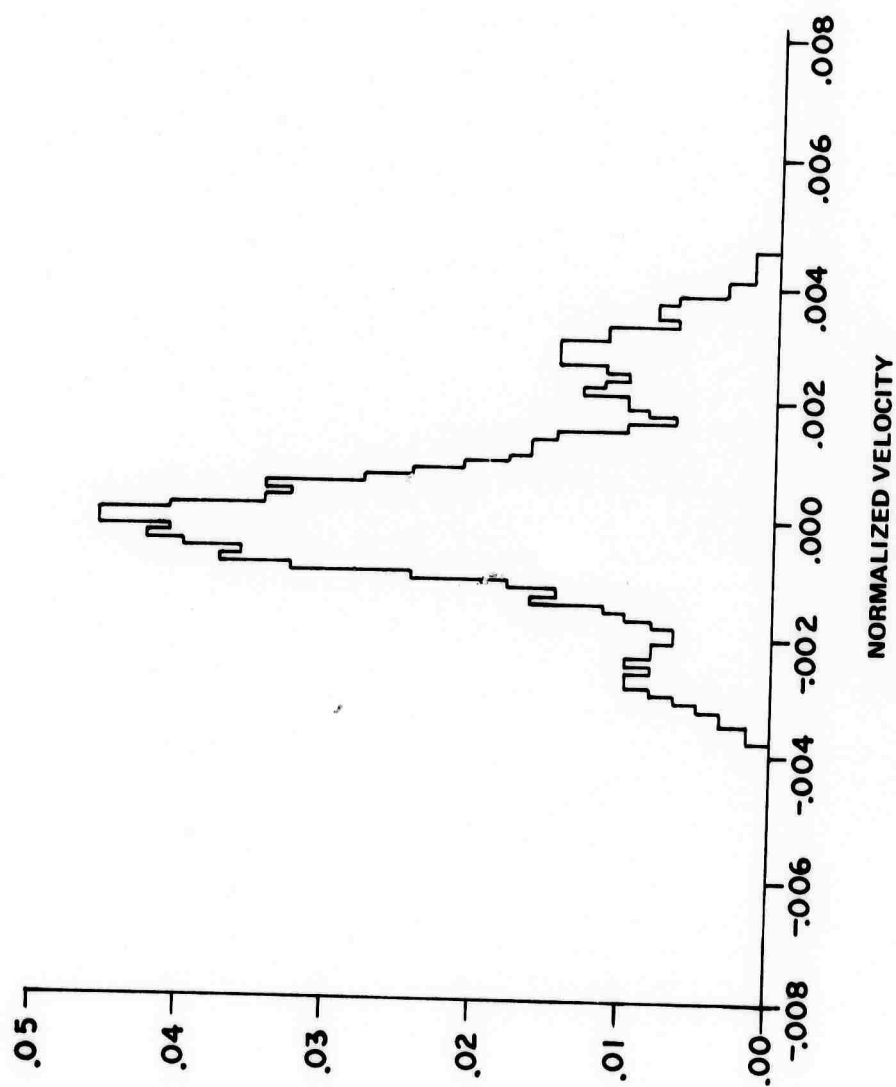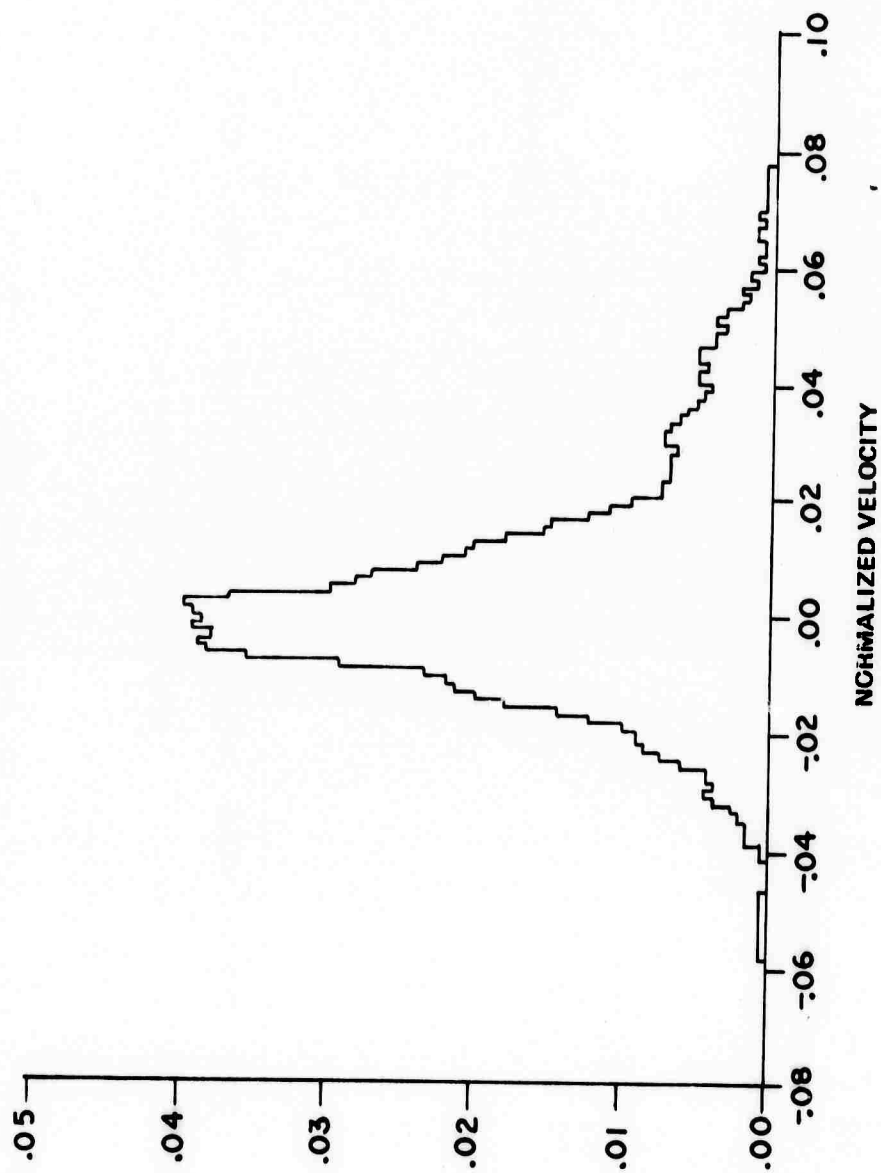Wake Position = 246 BD.

The origin of the double structure of the velocity histograms for the core data is not clear. The data base, while small, is still sufficiently large that one can believe that the feature is real. The persistence of the structure with time, and the near coincidence of the peaks when the velocity scales are normalized with respect to the standard deviation, lend additional support to the reality of the secondary peak. For the moment, and lacking further data, we must consider the question of the physical significance of the double structure (and perhaps its existence) an open one. The implications in terms of the Doppler spectrum of radar returns from re-entry wakes could be quite significant, but we will not examine them here.

2.2 TWO PARTICLE STATISTICS

Two particle dispersion statistics are of interest in the study of the distortion of fluid elements and stretching of fluid lines in a turbulent flow, and of turbulent mixing. Two particle data were generated under a prior program by systematically inserting pairs of particles in the wake, within a few millimeters of each other, and tracking the particle pairs.

A total of approximately 600 data runs were made to produce the data. However, the data could not be reduced at the time they were obtained, for lack of computer funds. Data reduction on the tests was delayed by about ten months, during which time the facility was dismantled and moved to a new location. This proved quite unfortunate, since attempts at data reduction undertaken in the present program were seriously hampered. Some tapes could not be processed or could be only fractionally processed because of an excess of parity errors which generally develop in tapes in prolonged storage. About 200 runs were lost in this manner. Of the data tapes that could be processed, some could not be reduced because the corresponding calibration data were missing. Finally, of course, some runs produced 'bad' data due to loss of particles from field of view, operator error. and so on. Naturally, there was no way to provide new calibration data, nor to produce more data.

The surviving data base, from which the results shown were derived, consists of only about 200 runs. This still represents a meaningful data base for a study of the general characteristics of two particle dispersion. It does not permit separation of the data into different classes by initial radial position, initial separation, and so forth. Note also that

the downstream distance coverage extends to somewhat less than a hundred and fifty body diameters (about two hundred and fifty drag diameters). This is because in a significant fraction of the data, one or the other particle of a tracked pair would leave the field of view beyond that distance. Retaining the remaining tracks would have introduced a systematic bias.

The principal features of interest in the two particle data, with respect to turbulent mixing and to the turbulent space time correlations, are the statistical properties of the separation vector of the two particles. We have derived results on both the two particle dispersion and the separation velocities, and these are discussed below.

For information purposes, typical trajectories of pairs of particles as generated by the data reduction routines are shown in Figure 9. The correlation of some of the trajectories, indicating organized eddies, is evident.

2.2.1 Two Particle Dispersion

The two particle dispersion statistics are shown in Figure 10, in which the axial, transverse. and total separation root mean square values are presented as a function of downstream distance.

The quantities plotted are $\left\langle Z^2(\zeta) \right\rangle^{\frac{1}{2}}$ and $\left\langle Y^2(\zeta) \right\rangle^{\frac{1}{2}}$ where Z^2 and Y^2 are defined respectively as

$$Z^2 = \frac{1}{D^2} \left[z_2(t) - z_1(t) \right]^2 \tag{8}$$

$$Y^2 = \frac{1}{D^2} \left\{ \left[y_2(t) - y_1(t) \right]^2 + \left[x_2(t) - x_1(t) \right]^2 \right\} \tag{9}$$

and z_i, y_i, x_i are the axial, vertical and transverse horizontal coordinates of the ith particle, D is the body diameter, and the transformation, $\zeta = U_\infty t/D$ from time to effective downstream distance, in body diameters, has been used.

The use of a single transverse dispersion $\left\langle Y^2 \right\rangle^{\frac{1}{2}}$ rather than separate horizontal and vertical dispersion is based on their observed equality (expected on the basis of axisymmetry).
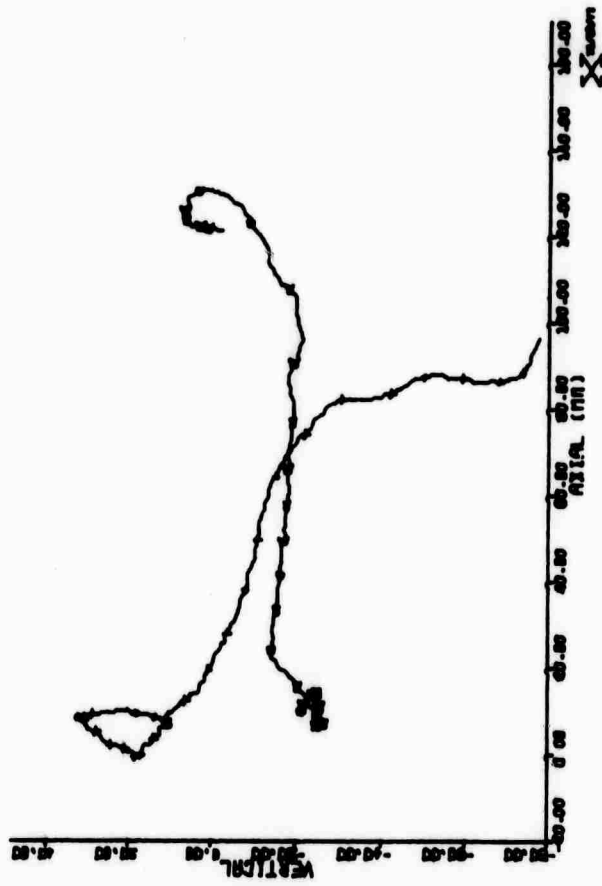
33
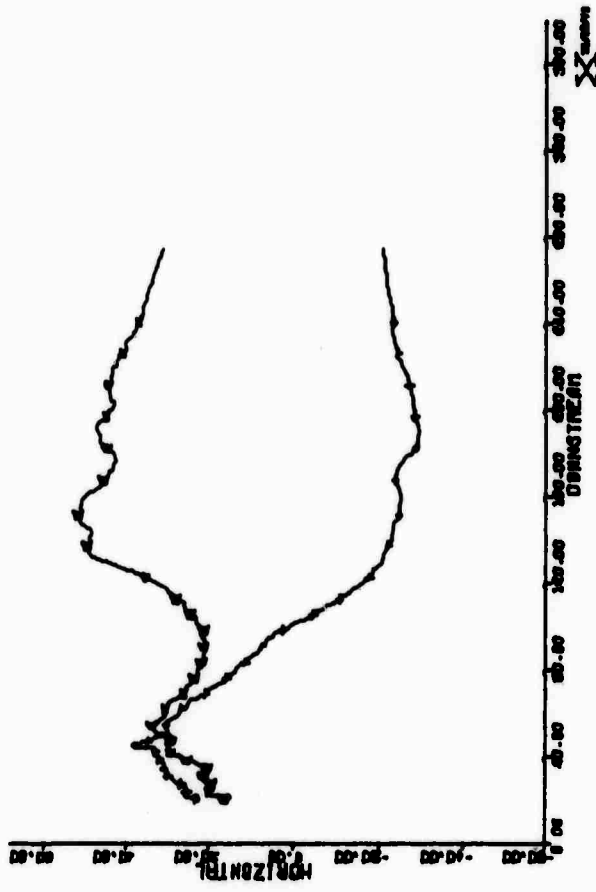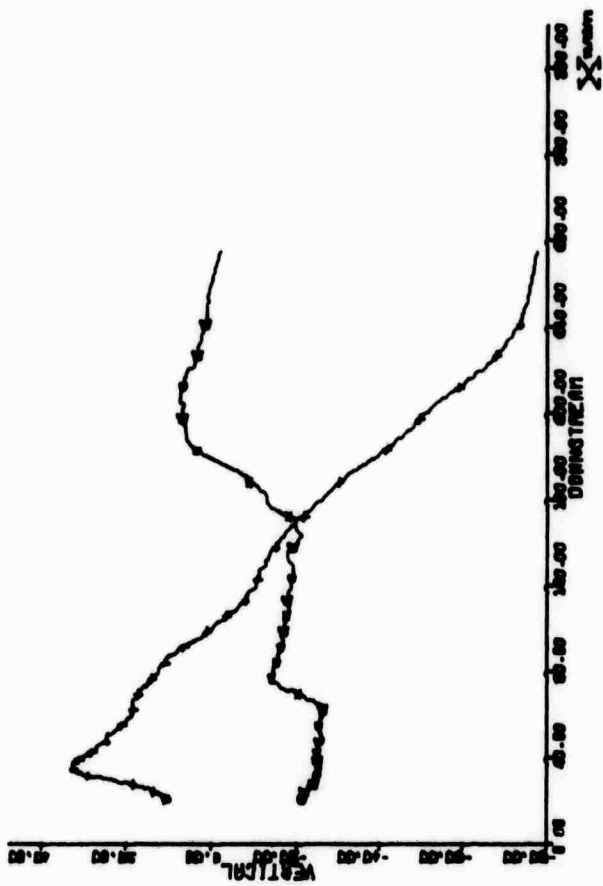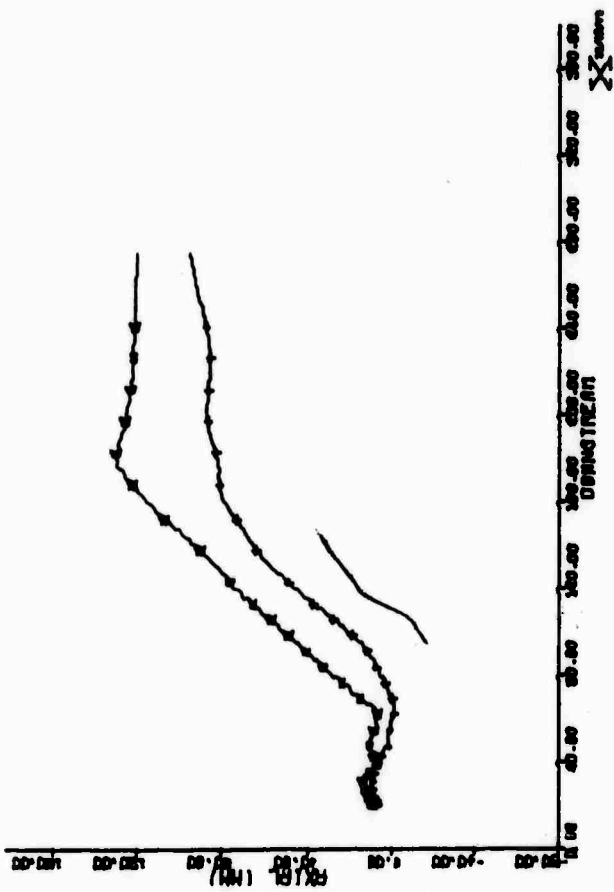
Figure 9a. Tape 217 – Tow 2.
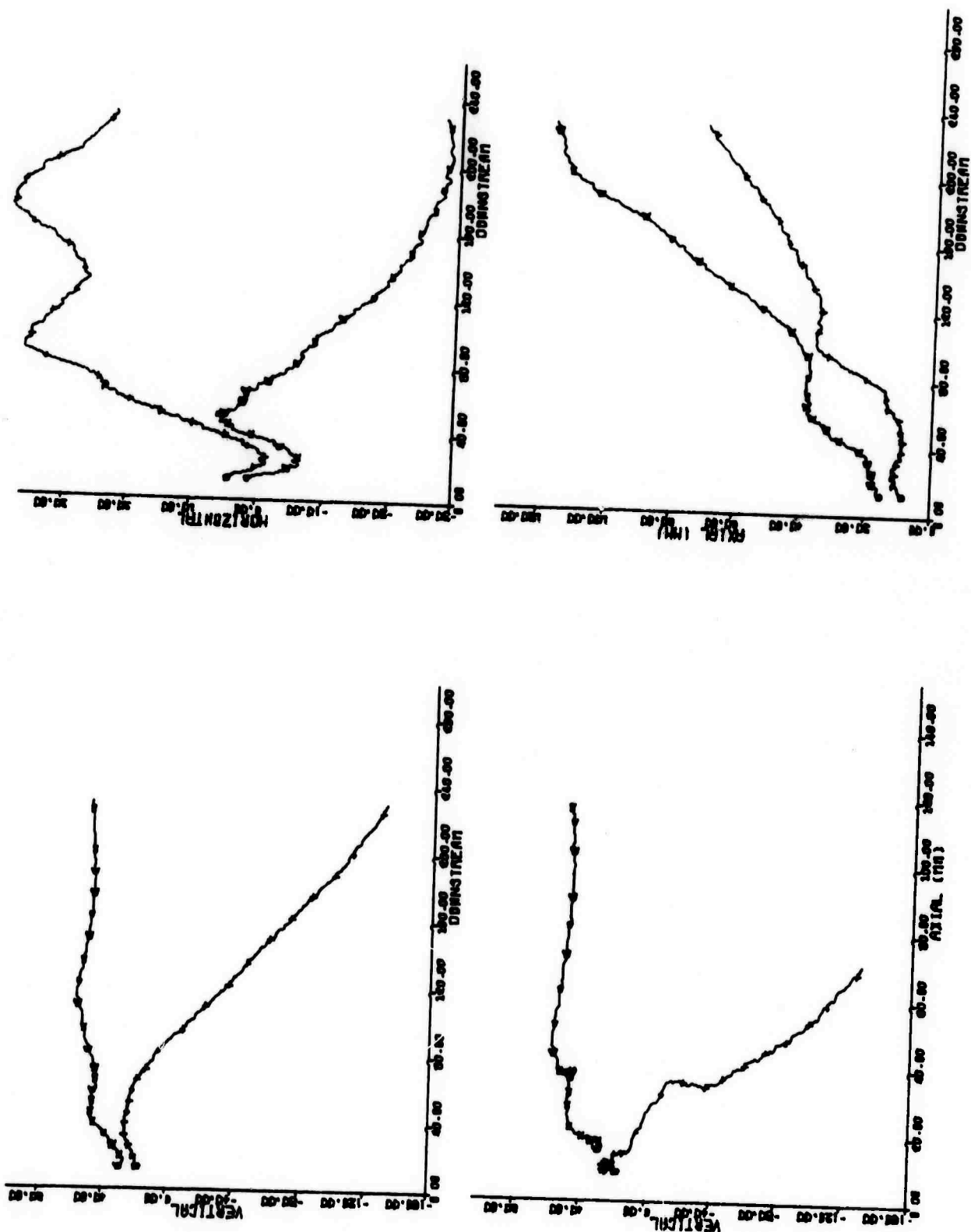
Figure 9b. Tape 217 – Tow 42.

Figure 9c. Tape 217 — Tow 96.

36
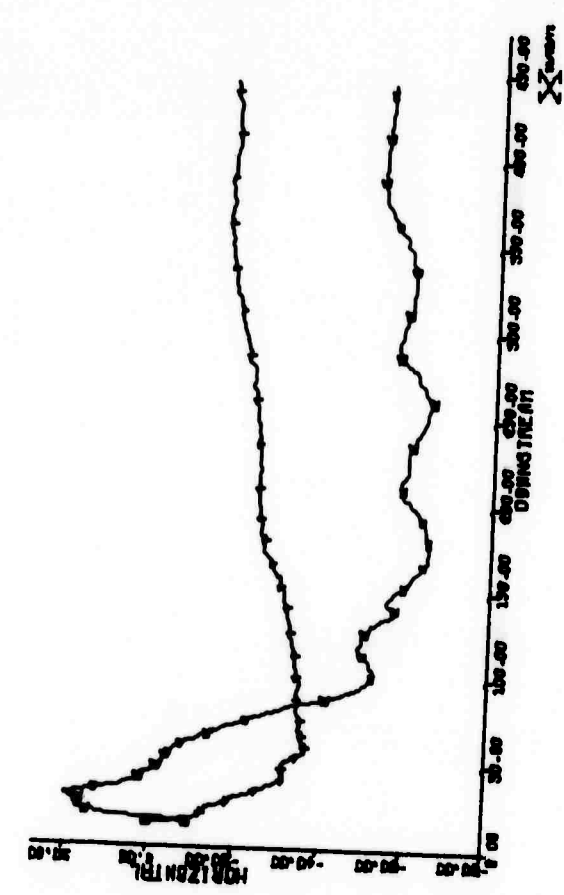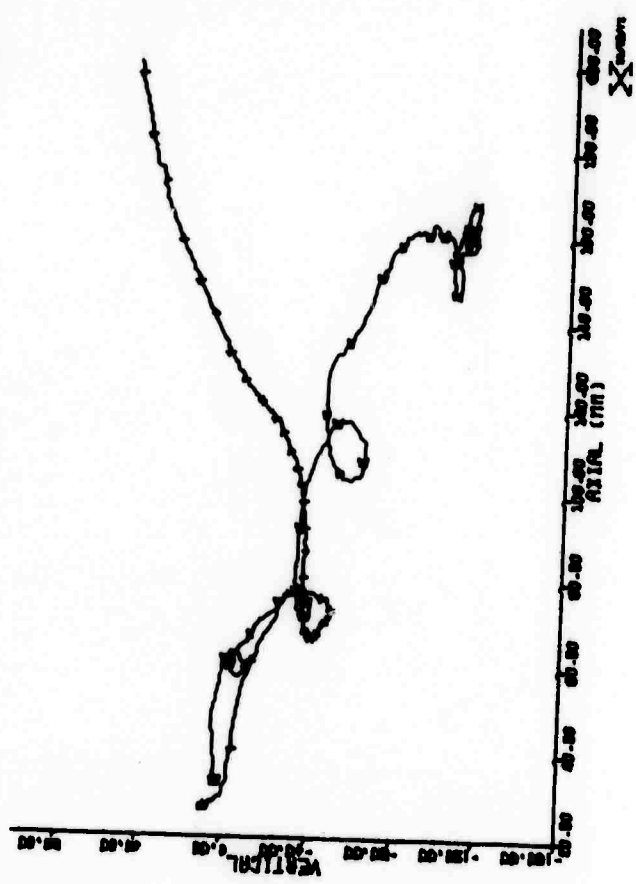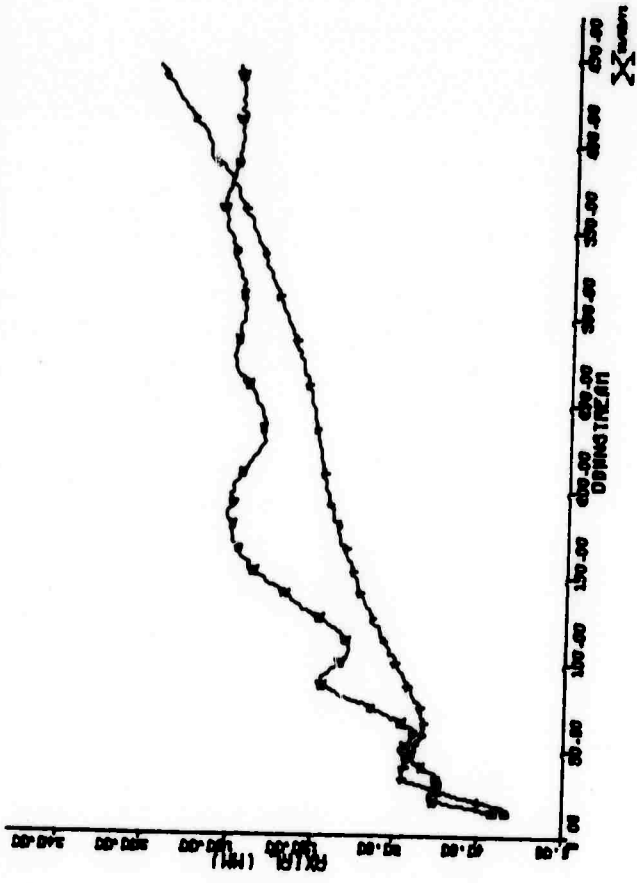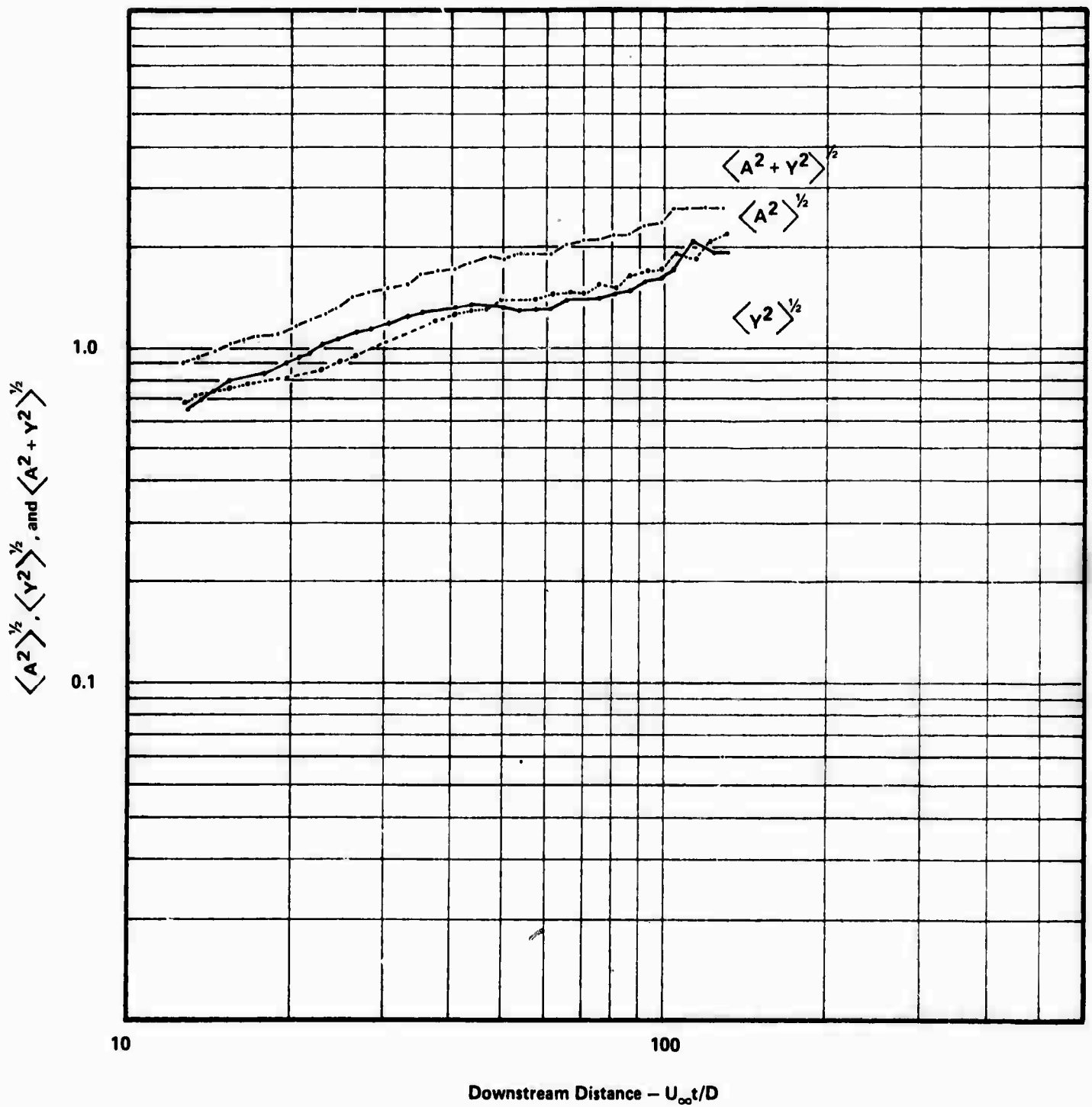
Figure 10. Axial, Transverse, and Total MSR Dispersion

37

Also plotted in the figure is the sum $\langle Z^2 + Y^2 \rangle^{1/2}$, which represents the total rms particle separation.

The first striking feature regarding the values of the transverse, axial and total root mean square particle separations are their large initial values. As previously noted[1], the experimental setup of the particle tracking apparatus leads to track acquisition at a downstream distance of approximately twelve to thirteen body diameters. At that point, as can be seen, the rms particle separation is approximately a body diameter, or around 4 cm. The initial rms particle separation is approximately one-tenth of a body diameter. Furthermore, visual observation of the experiments confirms that the large value of separation is not due to entrainment of one of the particles by the body. Indeed, when this occurs, the entrained particle is rapidly swept out of the field of view and the corresponding run is deleted. In addition, it is clear that the rms transverse and axial separations are equal from the outset, which would not be the case if the large separations merely reflected strong transverse gradients of axial velocity.[*]

The second notable semiquantitative feature of the two particle dispersion is the statistical equality, throughout the range of downstream distances measured, of the axial and transverse components of the two particle separation vector. Note that this does not imply isotropy, since the transverse mean square separation is the sum of the squares of the horizontal and vertical components. It indicates a mean turbulent effective rate of strain larger by $\sqrt{2}$ in the axial direction than in the other two orthogonal directions.

Quantitatively, the variation with downstream distance of $\langle Z^2 \rangle$ and $\langle Y^2 \rangle$ can be fitted, within our experimental accuracy, with a simple power law, of the form

$$\langle Z^2(\zeta) \rangle \simeq \langle Y^2(\zeta) \rangle \simeq 0.63\, \zeta^{0.92} \tag{10}$$

so that $\langle Z^2 \rangle$ and $\langle Y^2 \rangle$ grow approximately linearly with downstream distance or time. In a stationary flow, with constant mean square particle velocity, a linear mean square dispersion growth would represent a classical random walk. Thus, while the underlying

---

[*]*In interpreting the large values of particle pair separation at short distances behind the body, we should note that the initial particle separation, while small compared to a body diameter, is still large compared to the viscous dissipation scale, so that the significant velocity differences between the velocities of the two particles, implied by the large values of separation, can indeed be supported by the fluid.*

mechanism is undoubtedly different, still in a 'black box' so to speak, the rms particle dispersion behaves grossly like a classical diffusion with constant diffusivity!

In the wake flow, in which the rms velocity of each particle is decreasing, the above result implies an increasing rate of separation, measured with respect to 'total motion'. This qualitative behavior of two particle turbulent dispersion is well known in homogeneous (stationary) turbulence, in which Richardson's law[2]

$$\frac{d}{dt}\langle X^2 \rangle = A\epsilon^{1/3}\langle X^2 \rangle^{2/3}, \qquad \langle X^2 \rangle \gg \lambda^2 \tag{11}$$

can be 'derived' on the basis of the usual turbulence hypotheses, for values of dispersion large compared to the dissipation scale λ.

In Eq. (11), ϵ is the turbulent (kinetic energy) dissipation rate. In a non-stationary flow, one might expect a local form of Richardson's law, in which the local value of ϵ is used, to hold. From Eq. (11), we would then expect,

$$\epsilon \sim \frac{1}{\langle X^2 \rangle^2}\left(\frac{d}{d\zeta}\langle X^2 \rangle\right)^3 \sim \zeta^{n-3} \tag{12}$$

when $\langle X^2 \rangle \sim \zeta^n$,

where X stands for the axial or transverse dispersion Z or Y. Thus, in our case, from Eqs. (10) and (12), we would expect (since $n \simeq 0.9$)

$$\epsilon \sim \zeta^{-2.1} \tag{13}$$

This may be compared with the decay law for the turbulence dissipation rate found by Gibson et al[4] for a sphere wake

$$\epsilon \sim \zeta^{-2.35} \tag{14}$$

From the close agreement between the deduced value of Eq. (13) and the measured value of Eq. (14), we conclude that a local form of Richardson's law is obeyed by turbulent relative (two-particle) dispersion in the turbulent sphere wake.

39

We may further characterize turbulent dispersion by considering the velocities of relative motion, to which we now turn our attention.

2.2.2 Two Particle Velocities

The variation of the root mean square turbulent relative velocities, in the axial and transverse directions, defined as

$$\left\langle V_A^2 \right\rangle^{1/2} \equiv \left\langle (u_2 - u_1)^2 \right\rangle^{1/2}$$

$$\left\langle V_T^2 \right\rangle^{1/2} \equiv \left\langle [(v_2 - v_1)^2 + (w_2 - w_1)^2] \right\rangle^{1/2} \tag{15}$$

where u, v, w are the turbulent velocity components of each particle, are presented in Figure 11.

It may be seen that a simple power law again fits the data rather well. The best fit power laws yield

$$\left\langle V_A^2 \right\rangle^{1/2} \simeq 0.39 \zeta^{-0.68} \tag{16}$$

$$\left\langle V_T^2 \right\rangle^{1/2} \simeq 0.53 \zeta^{-0.66} \tag{17}$$

It is interesting to compare the variation of relative velocities, given by Eqs. (16) and (17), with the corresponding single particle turbulent velocity decays, which obey the approximate power law fits.[1]

$$\left\langle u^2 \right\rangle^{1/2} \simeq 0.53 \zeta^{-0.80} \tag{18}$$

$$\left\langle v^2 + w^2 \right\rangle^{1/2} \simeq 0.58 \zeta^{-0.77} \tag{19}$$

To compare the behavior of $\left\langle V_A^2 \right\rangle$ and $\left\langle u^2 \right\rangle$, we may note that

$$\left\langle V_A^2 \right\rangle = \left\langle u_1^2 \right\rangle + \left\langle u_2^2 \right\rangle - 2\left\langle u_1 u_2 \right\rangle \simeq 2\left\langle u^2 \right\rangle - 2\left\langle u_1 u_2 \right\rangle$$
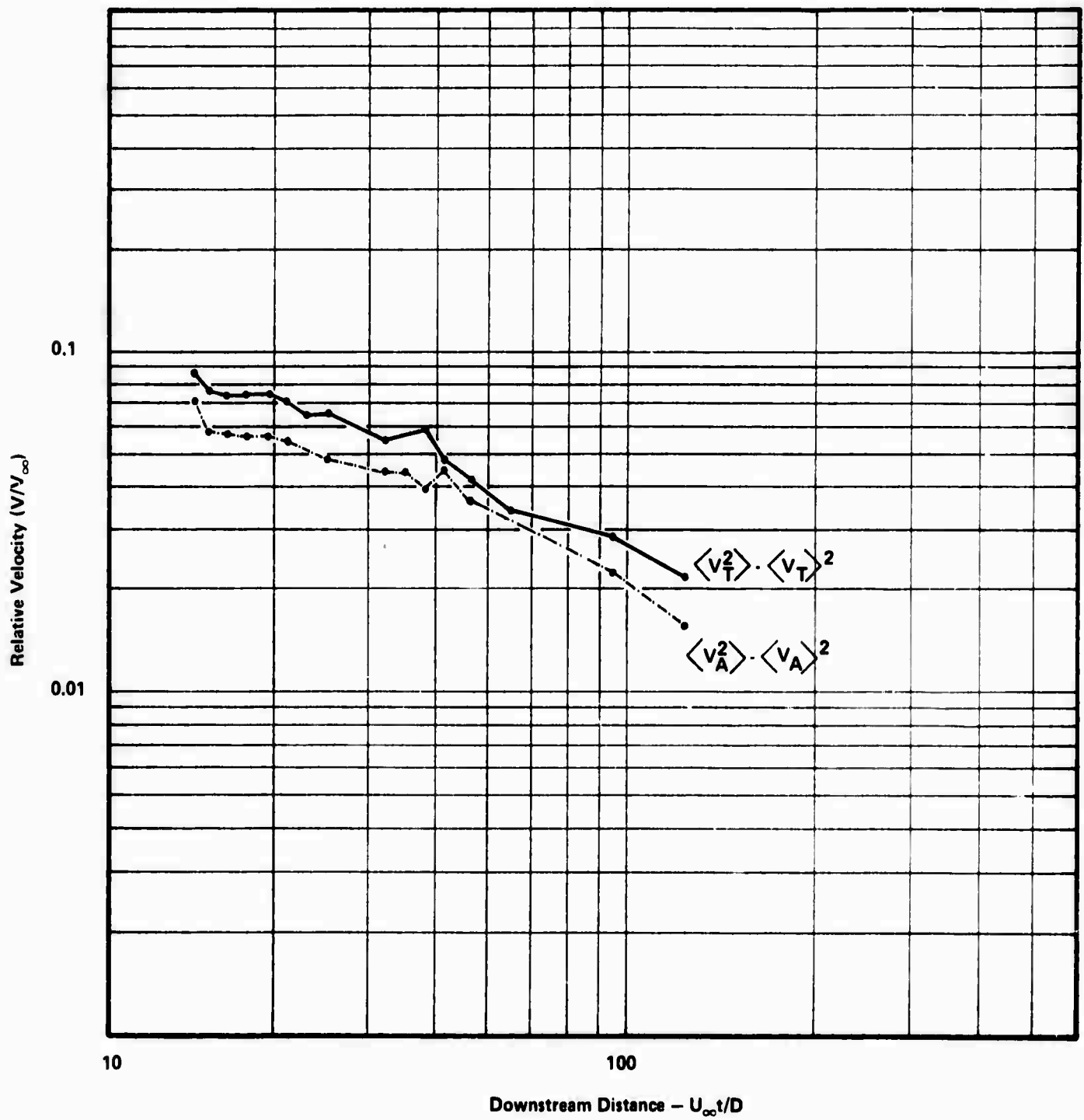
Figure 11. Axial and Transverse RMS Turbulent Relative Velocities.

so that $\langle V_A^2 \rangle$ should tend to $2\langle u^2 \rangle$ as the particle motions become uncorrelated, while of course $\langle V^2 \rangle \to 0$ when u_1 and u_2 are perfectly correlated.

It is clear from our data that $\langle V^2 \rangle^{1/2}$ is far from vanishing, although the ratio

$$\frac{\langle V_A^2 \rangle^{1/2}}{\sqrt{2}\langle u^2 \rangle} \sim 0.53 \, \zeta^{0.12} \tag{20}$$

remains somewhat below unity[*] up to downstream distances of approximately a hundred body diameters. We would conclude that the velocities u_1 and u_2 are weakly correlated, which is consistent with the observation that their root mean square separation is comparable to a body diameter over most of the tracked range of downstream distance. Similar results hold for the transverse velocities, as may be seen from Eqs. (17) and (19).

In addition to the relative velocity component fluctuations, another 'velocity' of interest in the two particle dispersion problem is the rate of separation of two particles, defined as

$$\dot{R} = \frac{\vec{U} \cdot \vec{R}}{|R|} \equiv \frac{(\vec{u}_2 - \vec{u}_1) \cdot (\vec{r}_2 - \vec{r}_1)}{|\vec{r}_2 - \vec{r}_1|} \tag{21}$$

that is, the rate at which the length of the segment joining the two particles increases (or decreases). The mean and standard deviation of $\dot{R}$, $\langle \dot{R} \rangle$ and $\left\{ \langle \dot{R}^2 \rangle - \langle \dot{R} \rangle^2 \right\}^{1/2}$ are shown in Figure 12.

From that figure, and by comparison with the single particle and relative turbulent velocity components, we note that the mean separation velocity is considerably smaller than the root mean square separation velocities or turbulent velocities, particularly at small values of downstream distance.

It is probably dangerous, considering the inadequate data base for the present experiment, to draw too much of a conclusion from this data, regarding the nature of turbulent diffusion in the wake. However, we cannot fail to note the following interesting

---

[*]*There is of course no fundamental reason why the ratio should not exceed unity; a larger than one ratio simply means that u_1 and u_2 are anticorrelated (i.e., $\langle u_1 u_2 \rangle < 0$).*
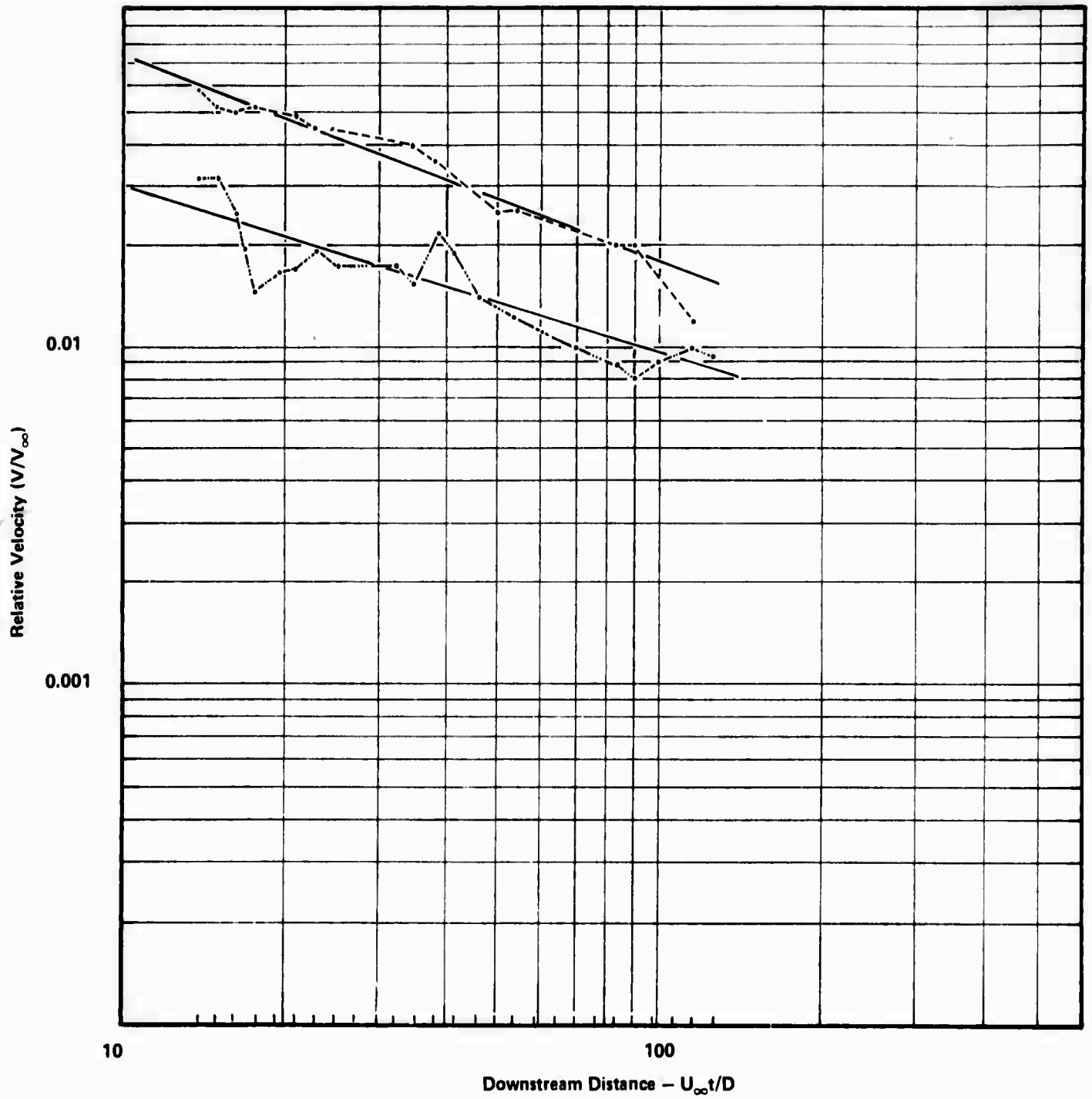
Figure 12. Mean and Standard Deviation of Total Separation Velocity

feature of the mean rate of separation: a power law fit (admittedly poor), yields a decay which is approximately

$$\langle \dot{R} \rangle \simeq 0.1 \zeta^{-0.5} \tag{22}$$

so that

$$\langle R \rangle = \int \langle \dot{R} \rangle \, d\zeta \simeq A\zeta^{0.5} \tag{23}$$

In other words, the Lagrangian mean separation, behaves (grossly) like a classical laminar diffusion with <u>constant</u> diffusivity!

The same approximate result was obtained regarding the growth of the root mean square particle separation $\langle R^2 \rangle^{1/2}$. Clearly, greater elucidation of this behavior would be central to an understanding of turbulent dispersion.

SECTION 3.

FACILITY DEVELOPMENT AND EXPERIMENT DESIGN STUDIES

As part of the current program, the Hydrodynamic facility was to be restored to operating condition, and enlarged so as to permit operation over a wider range of Reynolds and Richardson numbers, for stratified flow studies. Methods for density stratification of the water in the tank, using temperature stratification, and more generally design of momentumless wake experiments, including observation of surface currents generated by wake collapse, were to be undertaken. Those tasks were successfully completed and are described below.

3.1 THE NEW WATER TANK FACILITY

The water tank facility has been described in detail in previous reports[1]. During the contractual period covered by this report, the water tank facility has been restored to operational status in its new location at the Xonics Laboratories, and a number of modifications and additions have been made. Some of these changes represent minor, but valuable improvements dictated by past experience; others, such as the addition of a larger section to the tank, represent significant improvements aimed at expanding the capabilities of the facility, especially in the area of stratified fluid flows.

3.1.1 The Water Tank

The water tank is now 58 feet long, and is made up of ten sections (see Figure 13). The first six sections, representing a total length of 32 feet, have a five-by-five foot cross-section, and can be viewed from the bottom and one side through plexiglass windows. The last three sections, which represent a total length of 15 feet, also have a five-by-five foot cross section, but can be viewed on all sides through plexiglass windows.

The seventh section, which will be referred to as the middle or large section of the tank, was built during the present contractual period and was designed specifically for experiments in stratified media. This large section is 11 feet long and has a hexagonal cross-section whose dimensions are given in Figure 14. A sketch of the water tank, including the large section is given in Figure 13. The larger section has viewing windows on all sides.

A
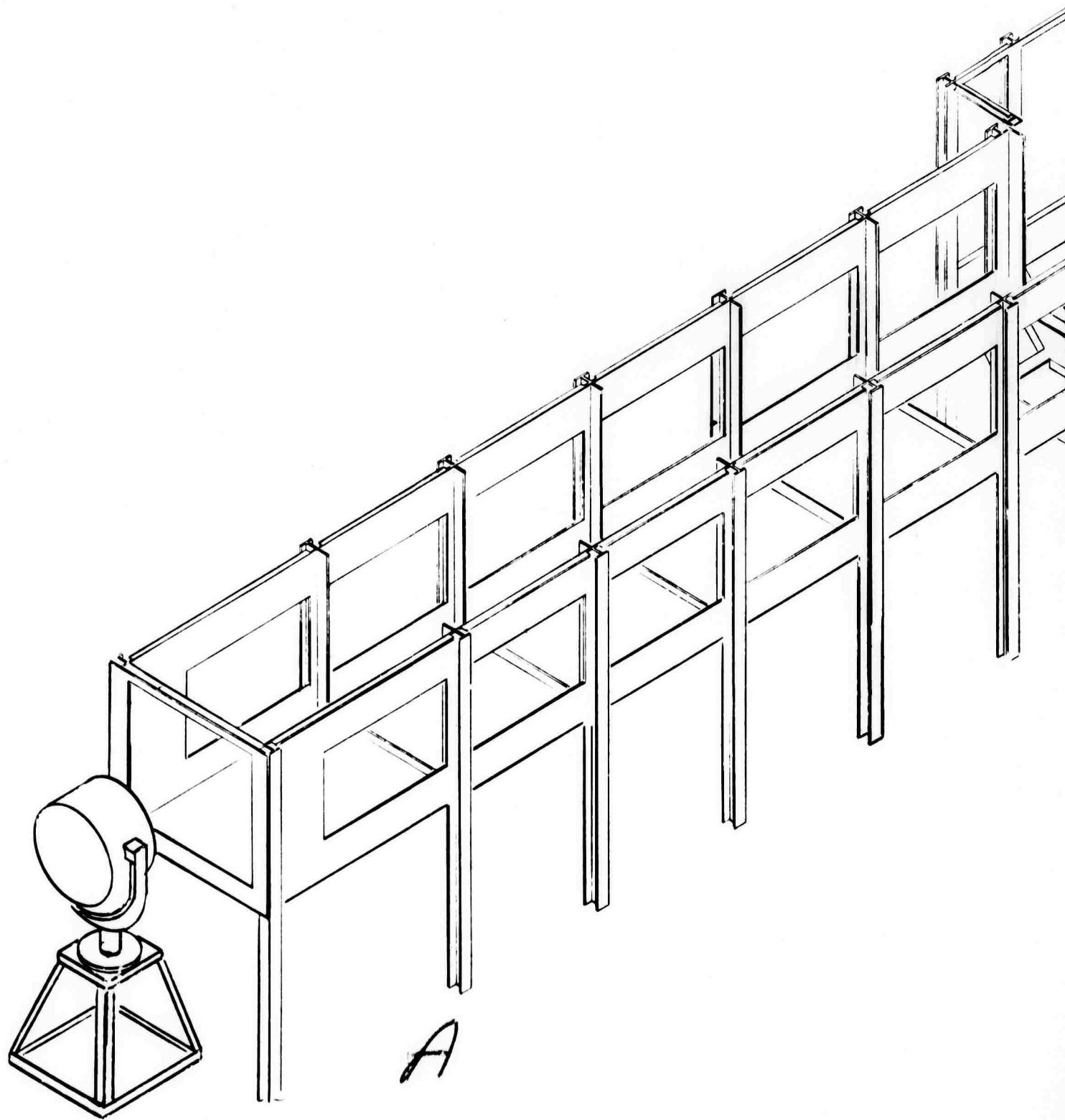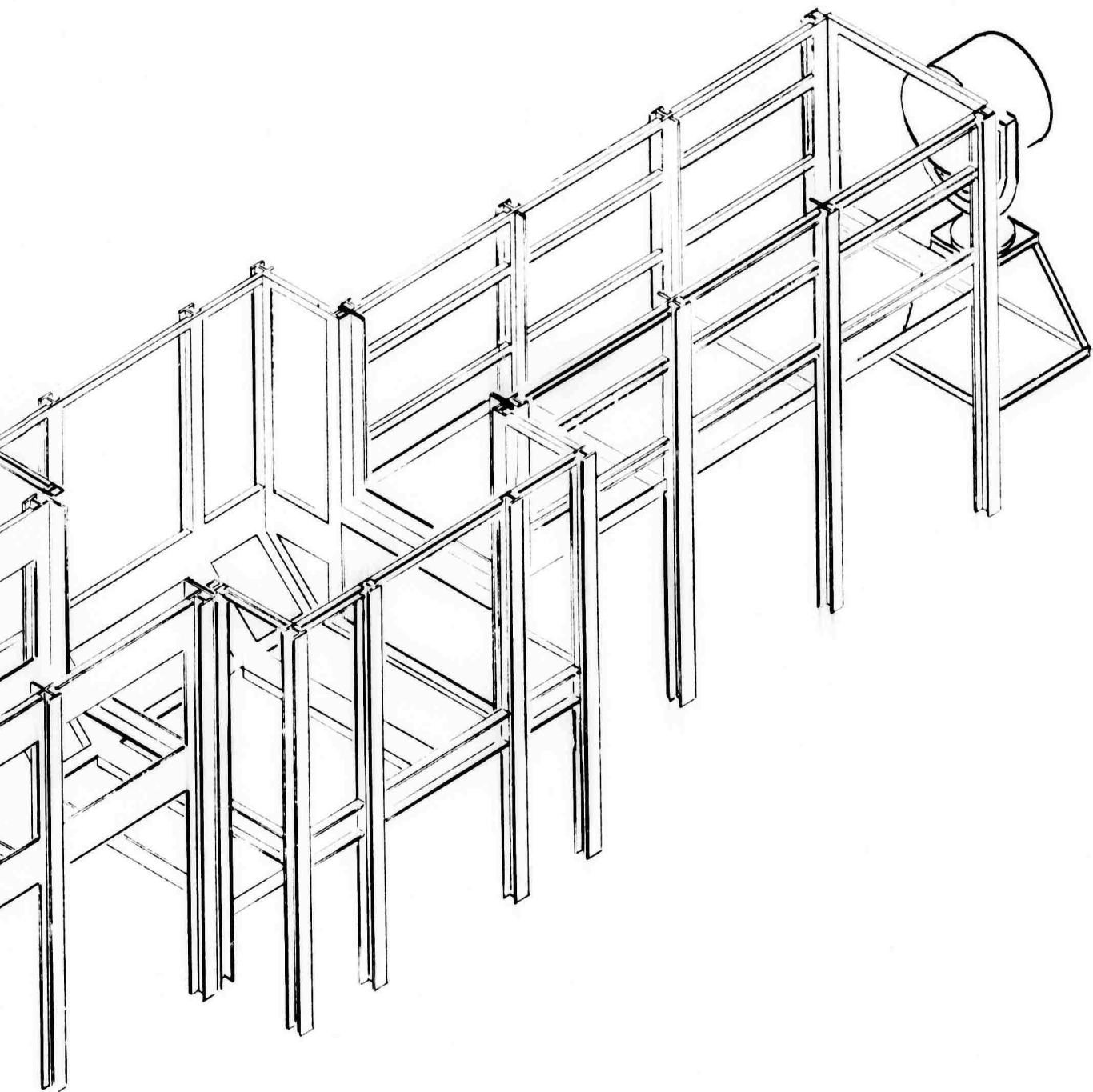
Figure 13. View of the Water Tank.
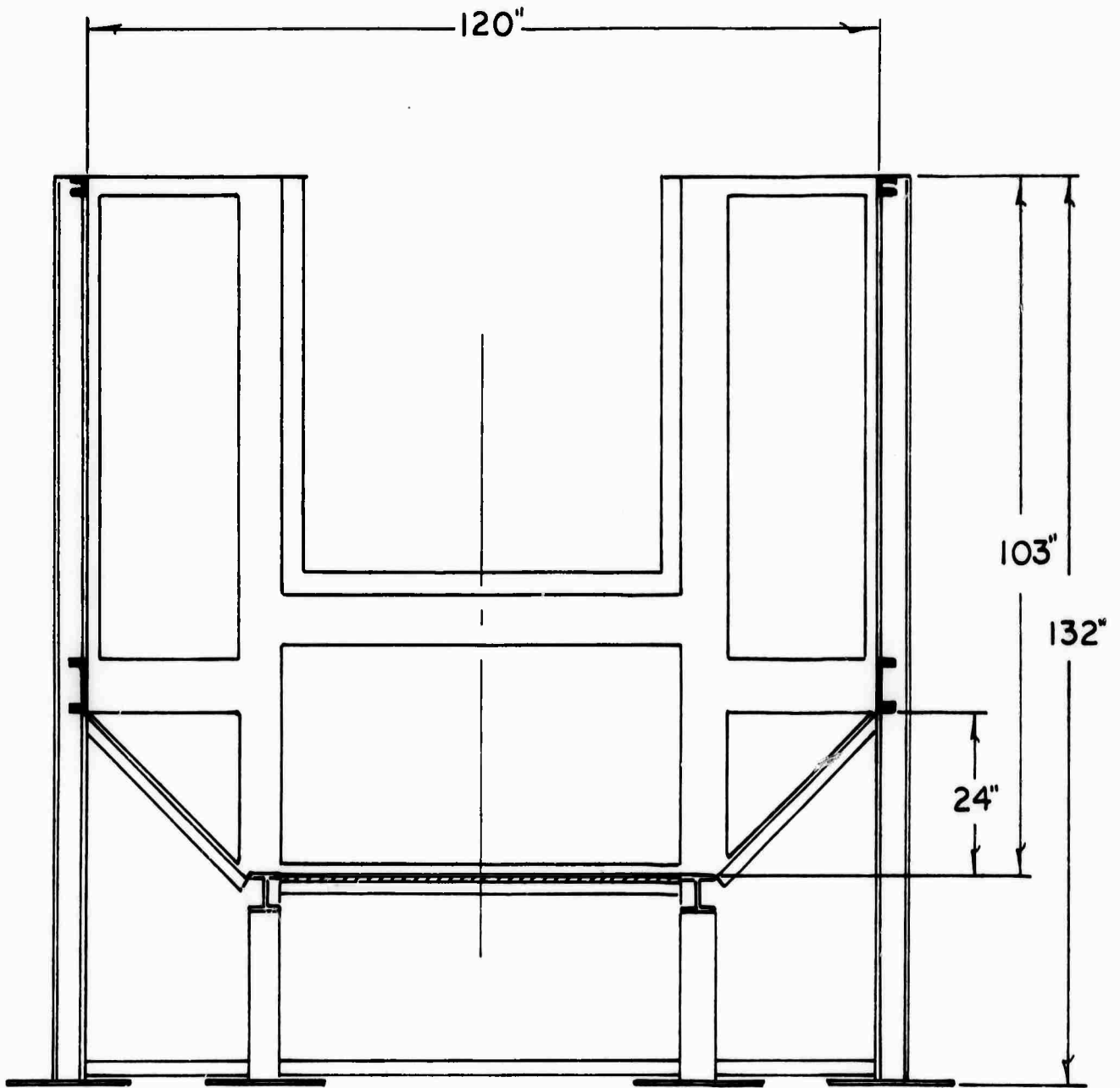
Figure 14. Large Tank Section.

47

The 1½ inch plexiglass windows are attached to the steel frame by means of rubber gaskets and stainless steel bolts.

The water tank, in its present configuration, is also provided with six inch wide separating flanges between sections, so that each section can be operated separately, i.e., can be isolated from the rest of the tank by means of steel or plexiglass plates bolted on the flanges. The interior of the water tank has been sandblasted and sprayed with a special anti-corrosive black plastic coating (Phenoline 302, manufactured by Carboline) to prevent contaminating the distilled water and preserve its initial high degree of clarity.

A "cat walk" was built along the entire length of the tank to provide easy access to the top working area of the tank. Moreover, the entire facility is enclosed in a 70' x 28' room which will be temperature controlled and air filtered using electrostatic filters attached to the air-conditioning system. To prevent unwanted reflections during operation, the walls, floor, tank, and most of the supporting equipment have been painted black.

3.1.2 The Plumbing System for Stratification

The plumbing system has been radically changed to a more efficient and versatile one. It allows now for independent filling and evacuating of each section of the tank. Moreover the system has been designed to (a) generate a thermally stratified medium in a chosen test section, starting with room temperature distilled water, (b) efficiently regenerate the stratification after mixing has taken place, and (c) clean and filter the water in the whole tank or sections of it.

A more detailed description of the operations performed by the plumbing system, as well as the temperature stratification technique will be given in Section 3.2.

At present, a reduced version of the system, including the stratification generator has been completed and operates on the first six sections of the tank.

3.1.3 Illuminating System

The illuminating system consists of a pair of commercial Mole Richardson air cooled projectors, equipped with 5 Kw Hanovia Xenon mercury high pressure arc lamps. Placed at each end of the tank, they provide a collimated beam of light with an effective diameter of 33 cm. This beam of light illuminates the tracer particles, which are 0.5 mm diameter neutral density polystyrene particles, and which are introduced in the chosen

48

test area by means of one or more hollow glass tubes connected to rubber squeeze bulbs filled with particle-laden water.

3.1.4 The Optical Tracking and Recording System

A new optical scanning system has been designed and is described in Appendix B. At present the previous scanning system has been restored to operational status. A detailed description of the functions performed by the optical tracking system was given in a previous report[1]. Basically optical tracking is achieved by the use of an optical system which images a particle through four separate systems of mirrors and lenses and permits tracking of the projected motion of the particles into four directions; and a rotating slit system on the scanner which permits the digital counting of the particle displacements. The scanner consists of an optics plate on which are mounted most of the mirrors and lenses, a rotating drum containing seven slits, and the housing on which are mounted four photomultipliers (one for each direction).

The particle tracking is most readily described as follows: a given slit in the rotating drum of the scanner exposes a thin strip of photomultiplier to light emanating from the illuminated volume. The slit and lens center define a plane which is imaged into a plane in the towing tank. As the drum rotates this plane rotates out of the lens center and thus sweeps the viewing volume. The angular position of the "tracking slit" on the drum is measured by counting time digitally between a reference pulse and the particle pulse. The output of each photomultiplier is filtered, amplified then sent to a discriminator which produces a fixed 10 volt pulse for every input pulse above a certain level. The pulses are sent to a multiscalar control logic which receives reference pulses also from a start-stop system, which acts as a control for the logic. The data are transferred and stored serially in a memory and then stored on digital magnetic tape for processing.

The mapping from the photomultiplier pulses into particle coordinates is achieved by measuring the rotational angle θ of the slit between a reference pulse (corresponding to a reference position in the tank) and a particle pulse. The angle θ defines a plane in which the particle is located. The intersection of the three orthogonal x, y and z planes define the portion of the particle and the fourth plane is used as a check to remove ambiguities (ghost particles).

3.2   MOMENTUMLESS WAKE EXPERIMENT DEFINITION

A study was conducted to define the feasibility of a momentumless wake experiment in a thermally stratified medium. Basically the measurement technique to be adopted is identical to the previous technique used in the study of turbulent wakes of towed bodies in a homogeneous medium. It consists of measuring Lagrangian histories of fluid particles by tracking tracer particles. The principal innovative features of the new experiment setup are:

(1)   The generation of a stable thermally stratified medium.

(2)   The design and construction of properly guided self-propelled bodies. .

(3)   Modifications of the present scanning system.

3.2.1   The Temperature Stratification Technique

The most important part of the modified experimental setup is the generation of a stable thermally stratified medium (water). An experiment definition study was undertaken to determine, among other things, the most effective and economical way of achieving thermal stratification in water. A simple and very effective method was devised as a result of this study. It consists of depositing successively hotter layers of water through a floating system of screen. Figure 15 depicts the principle and the actual configuration of a small scale experiment which was performed in a 42 inch long, 30 inch wide and 36 inch high plexiglass water tank. Water at the desired temperature is deposited over a pair of parallel screens, one centimeter apart, by means of an array of evenly spaced bubblers (6 in the actual experiment). The screens fulfill two purposes: (a) they evenly distribute the water over the whole surface, and (b) they essentially reduce to zero the velocity of the water so that mixing due to forced convection is minimal.

Six layers of water, each approximately three inches thick, were deposited using the floating screens. The chosen temperatures of the layers were, in increasing order: 70°, 90°, 105°, 118°, 131°, 138°(f) and the corresponding relative variation of the density from one layer to the next was about 0.3%.

Red and blue dyes were introduced in the third and fifth layers, respectively, and pictures were taken at intervals of about half an hour, starting after the stratification was completed. The boundaries between layers were sharp, and no convection currents were visible except near the surface of the water, where convective diffusion due to the cooling
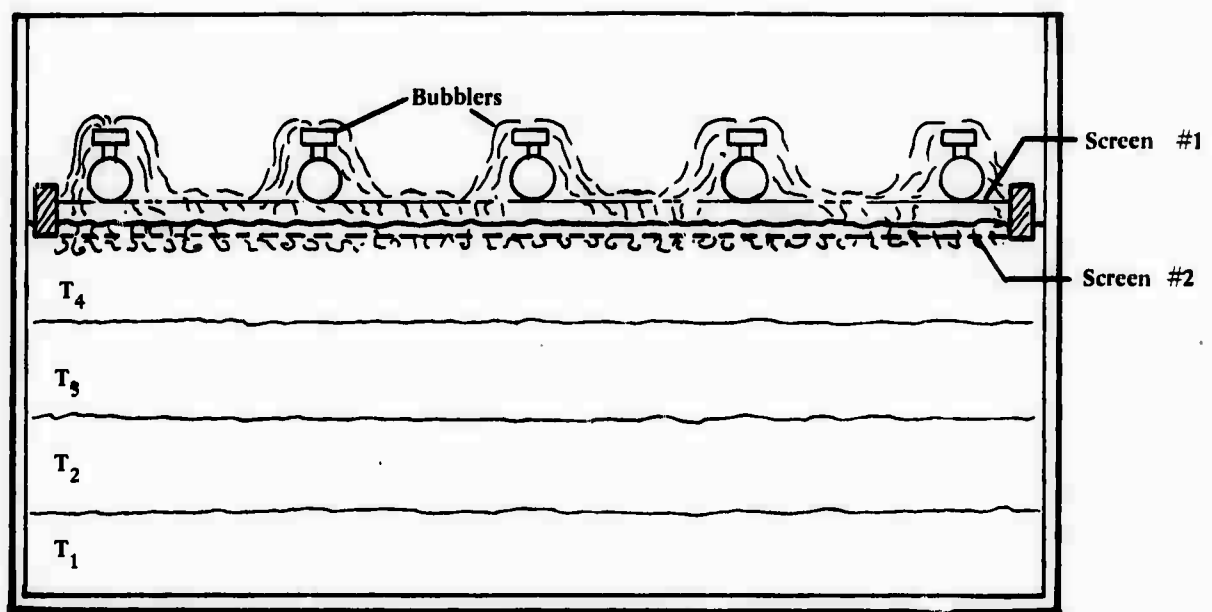
Figure 15. Schematic of Temperature Stratification System.

of the surface accelerated the diffusion of the blue dye into the sixth layer. After about
two hours, the blue dye was uniformly distributed in the last two top layers of water.
This problem can nonetheless be easily corrected by covering the tank to prevent
evaporation.

Temperature measurements of the water were made, using a thermocouple probe,
at intervals of about one hour. The temperature profiles versus depth (Figure 16) deviate
very little from a linear equilibrium profile.

Similar experiments were carried out, full scale, in the hydrodynamic tank, and
again, controlled profiles were readily generated. A typical profile is shown in Figure 17.

A detailed description of the plumbing system required to obtain and regenerate
thermal stratification in the water tank follows.

Reference to Figure 18 may be helpful in understanding how the plumbing system
works. Each pump is in series with two filters and these units are manifolded to the water
heater, water cooler, thermostatic mixing valve, and the tanks to perform the required
tasks.

The stratification generator float (see Figures 19 and 20) consists of two layers
of styrofoam separated by fiberglass screens and having a bubbler array on top of this.
The float arrangement insures the development of even temperature layers since very little
mixing occurs because the water trickles through with very little energy.

When it becomes necessary to re-stratify the test section, the float will be weighted
so that the bubbler heads are just below the water level. The water will be removed in
layers and shunted to storage tanks using the same techniques and equipment as was used
to fill the test section. The system as designed is for manual operation but is readily
adaptable to programmed operation.

3.2.2 Self-Propelled Vehicle

The momentumless vehicles are shown in Figures 21, 22 and 23. All the test sub-
jects will be balanced to neutral buoyancy.

The laser guided model follows a very narrow beam from a helium neon laser
(typically less than 1 mm in width and having a divergence of less than a milliradian). A
narrow bandpass filter in front of the diode quad rejects all light except the 6328Å light
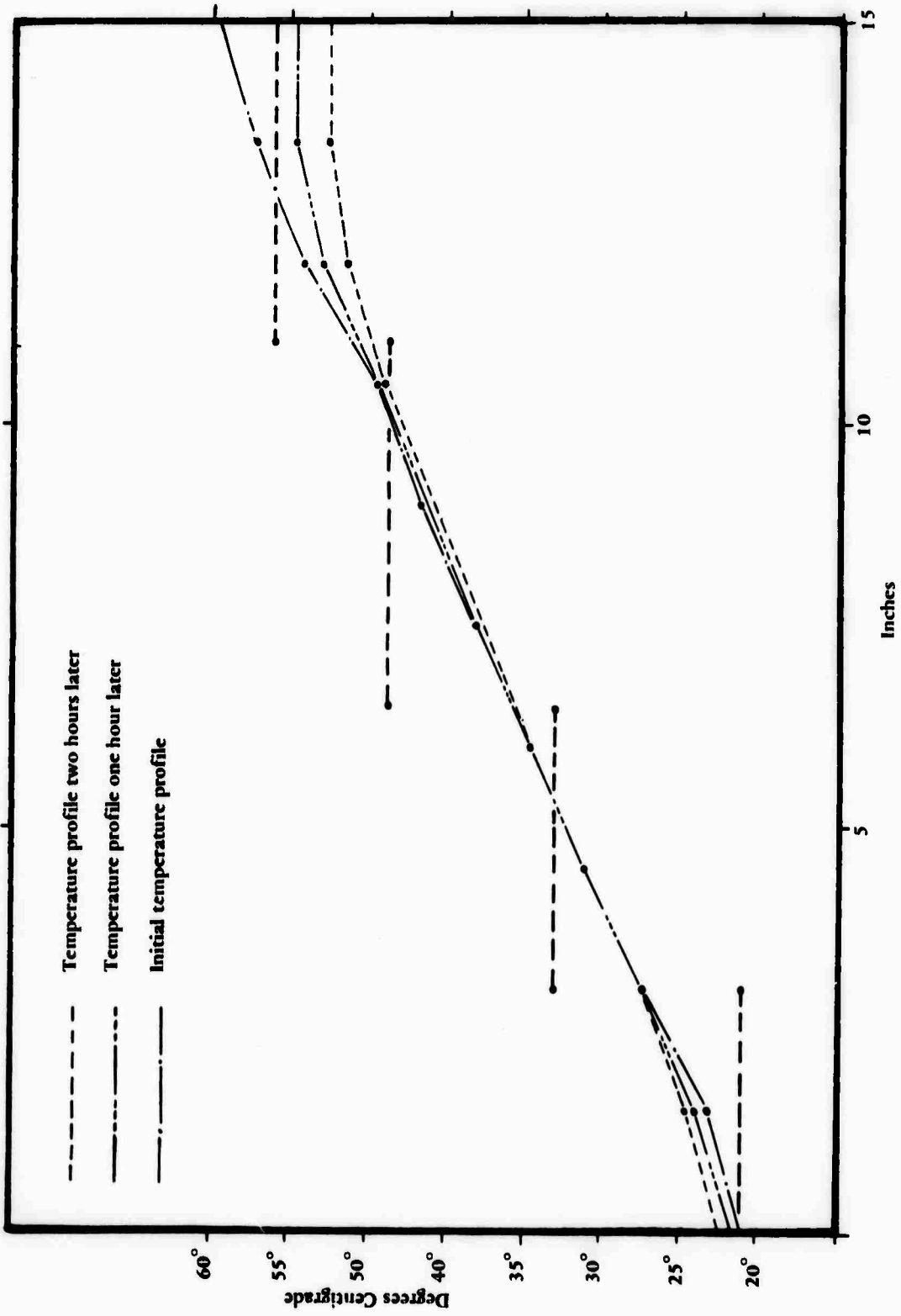
Figure 16. Temperature Profile versus Depth.

Temperature profile two hours later
Temperature profile one hour later
Initial temperature profile

Degrees Centigrade

Inches

60°
55°
50°
45°
40°
35°
30°
25°
20°

5
10
15

53
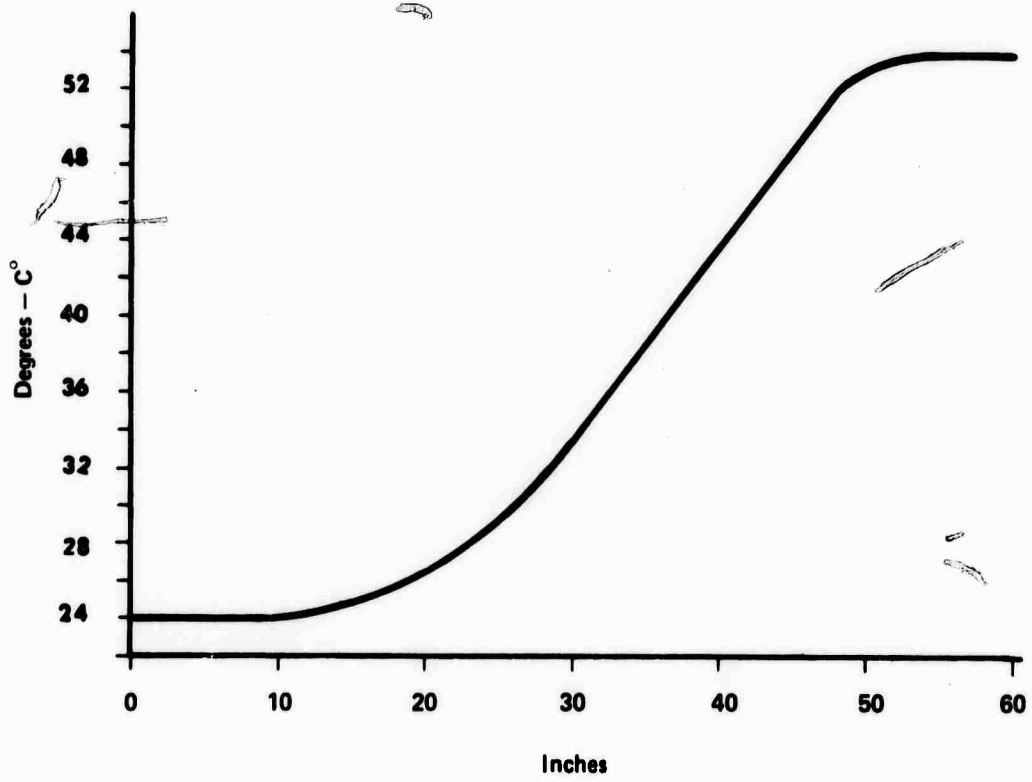
Figure 17. Temperature Profile versus Depth.
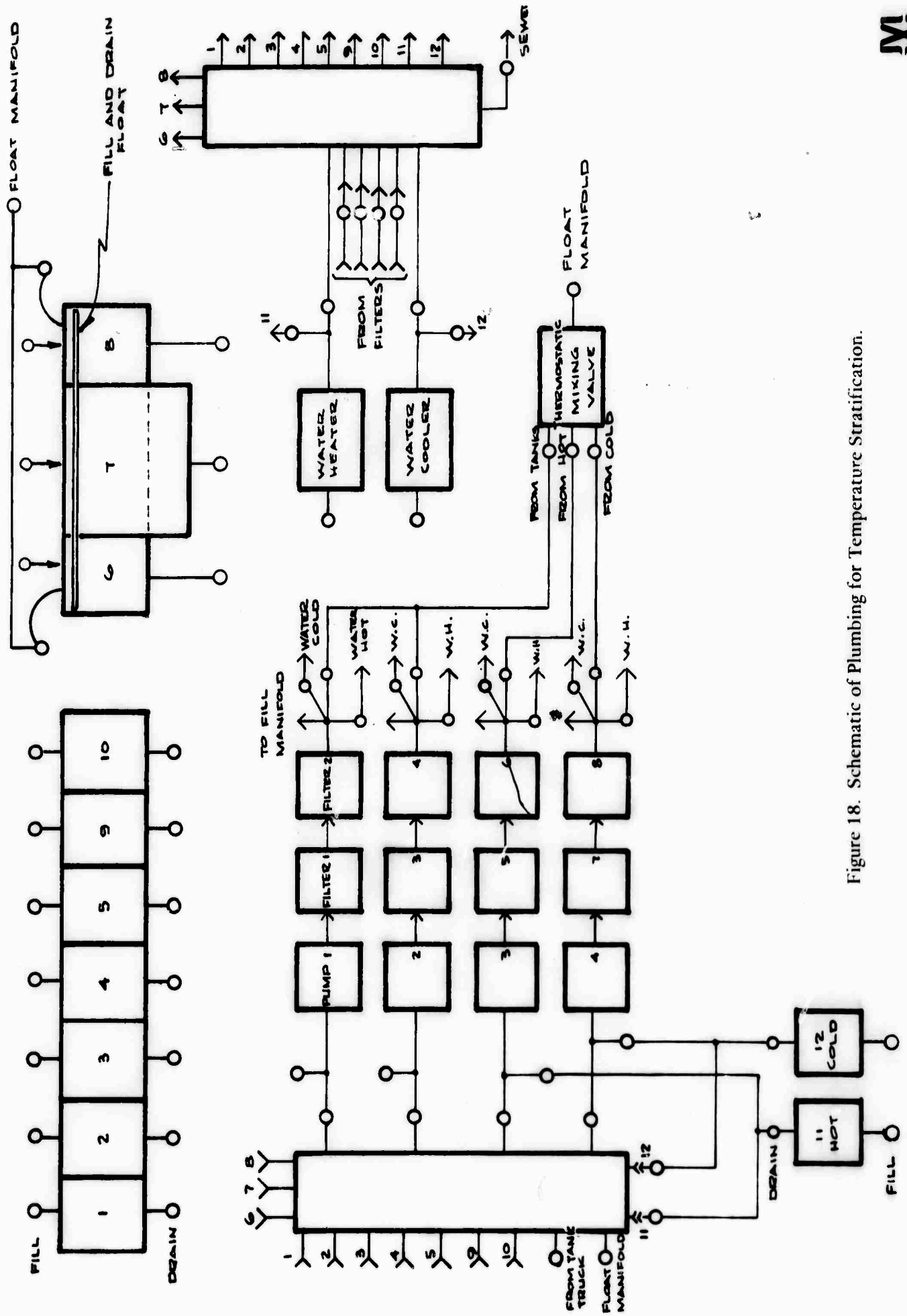
Figure 18. Schematic of Plumbing for Temperature Stratification.
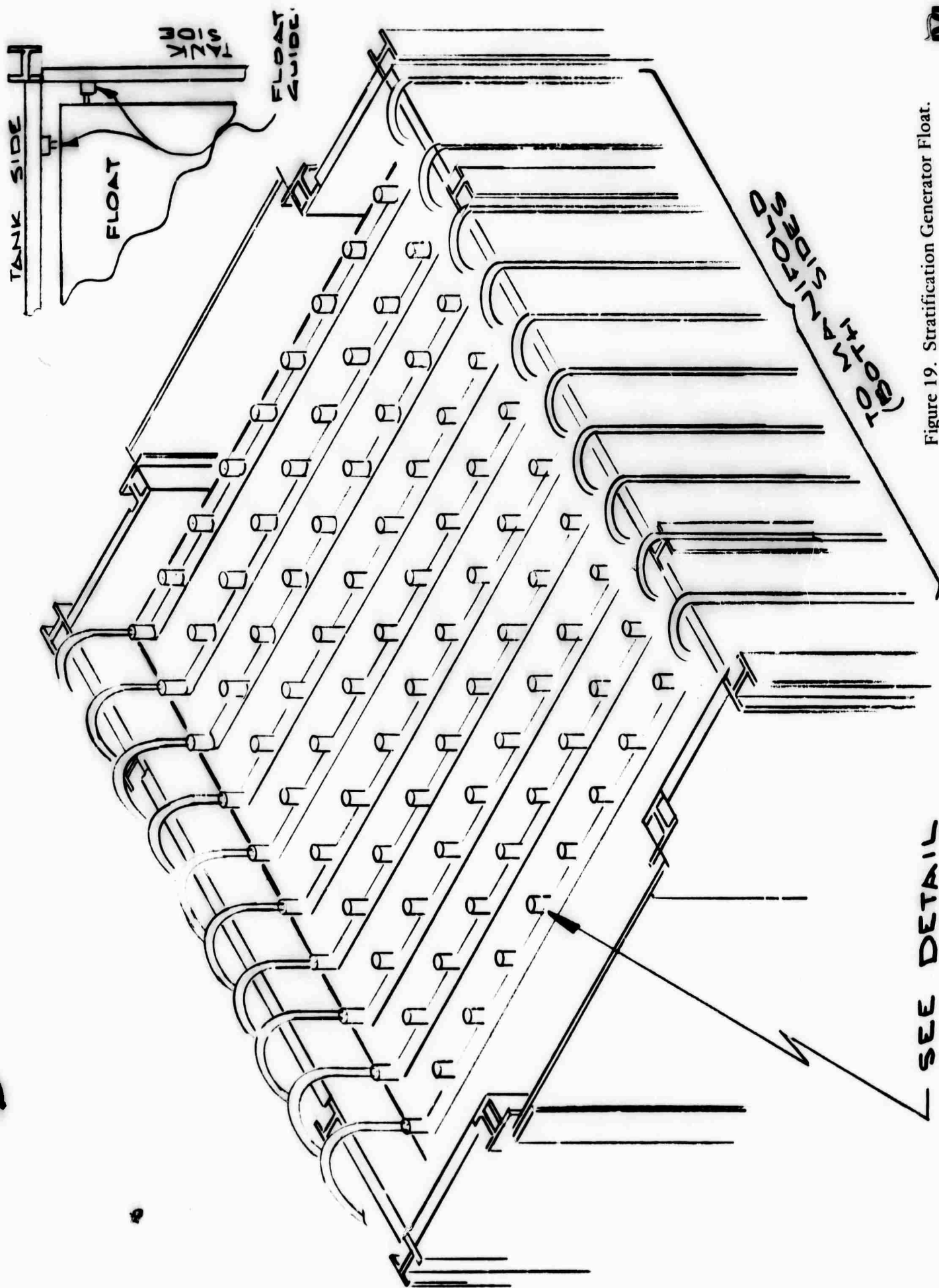
Figure 19. Stratification Generator Float.

TANK SIDE

FLOAT

FLOAT GUIDE

TANK SIDE

BOTTOM SIDE
(DISTRIBUTOR)

SEE DETAIL
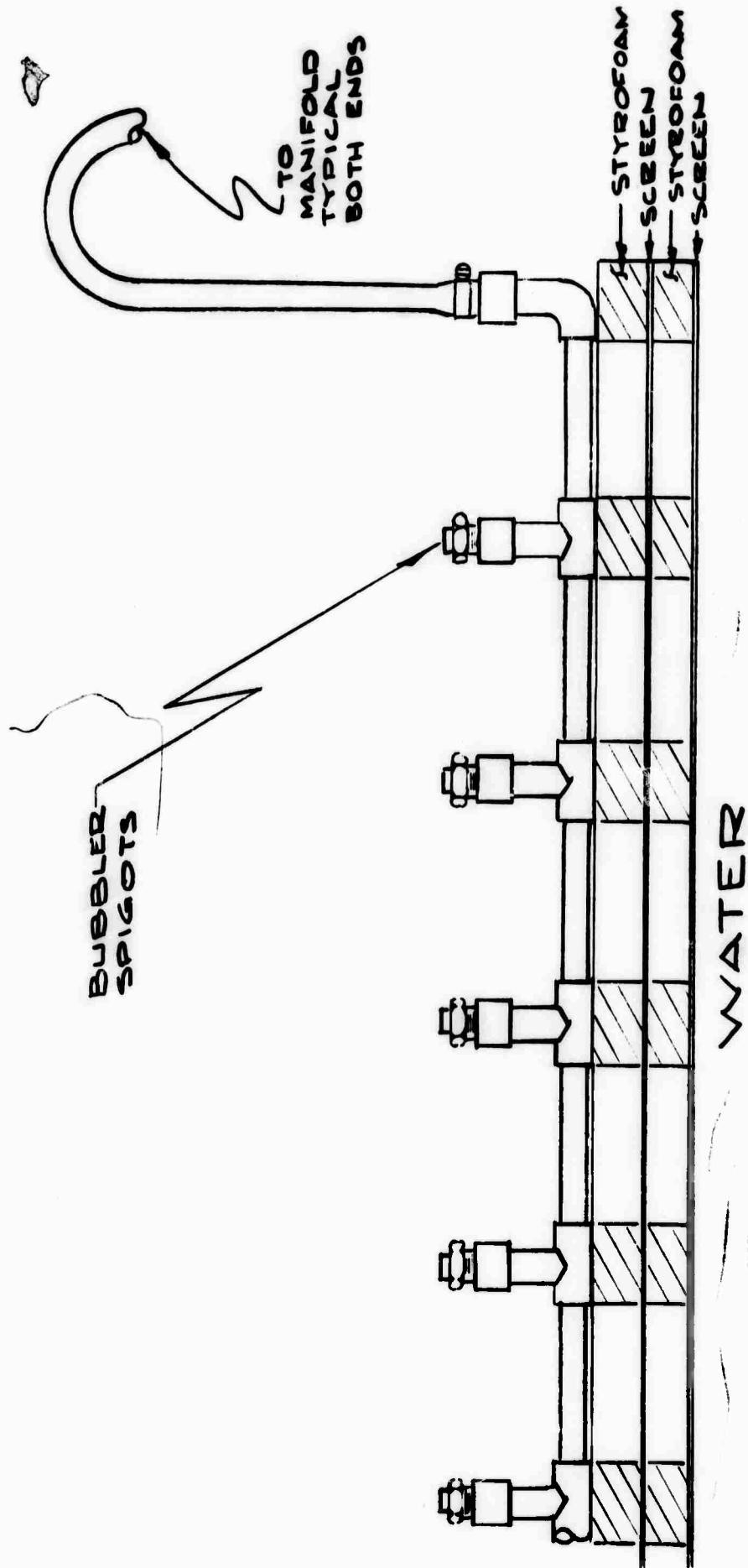
Figure 20. Stratification Generator Float – Detail.

TO MANIFOLD TYPICAL BOTH ENDS

STYROFOAM
SCREEN
STYROFOAM
SCREEN

BUBBLER SPIGOTS

WATER
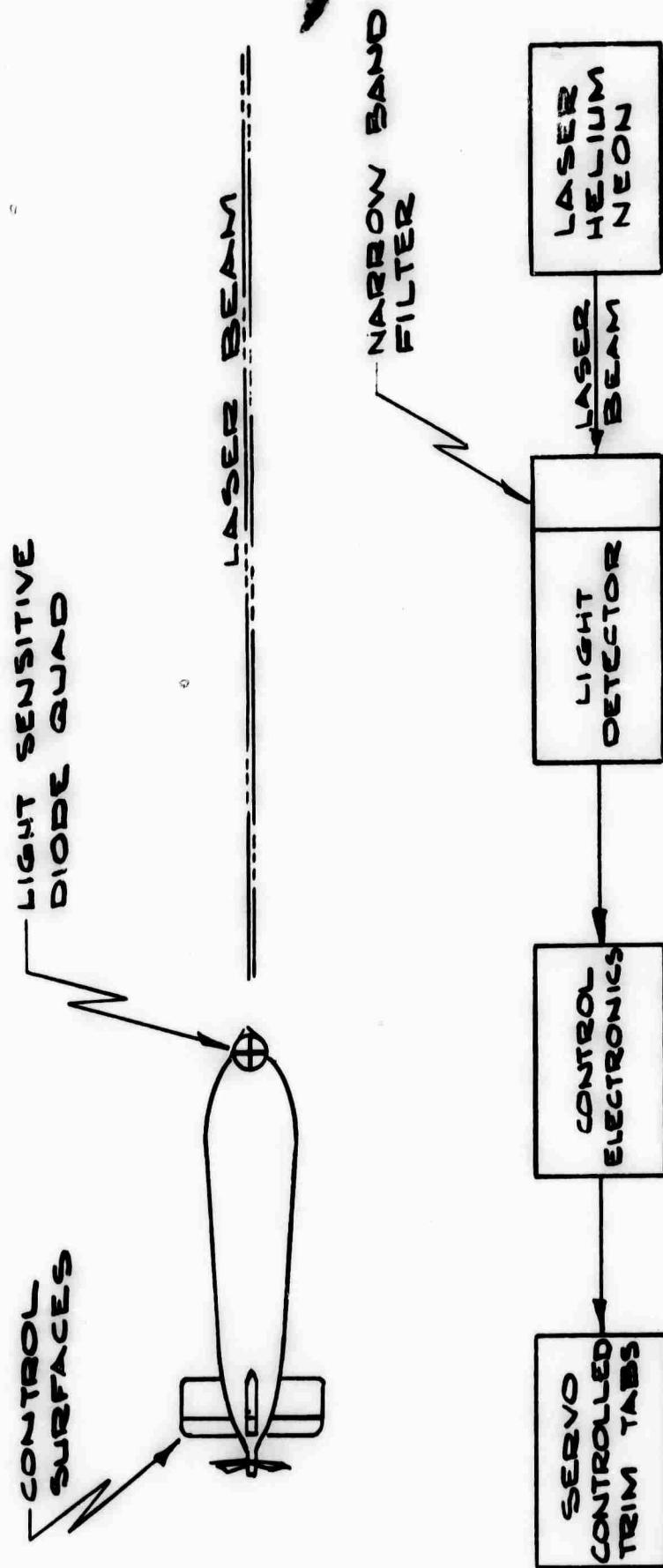
Figure 21. Momentumless Vehicle, Laser Guided (Internal Battery Power).

NON REFLECTIVE WIRE

PROP
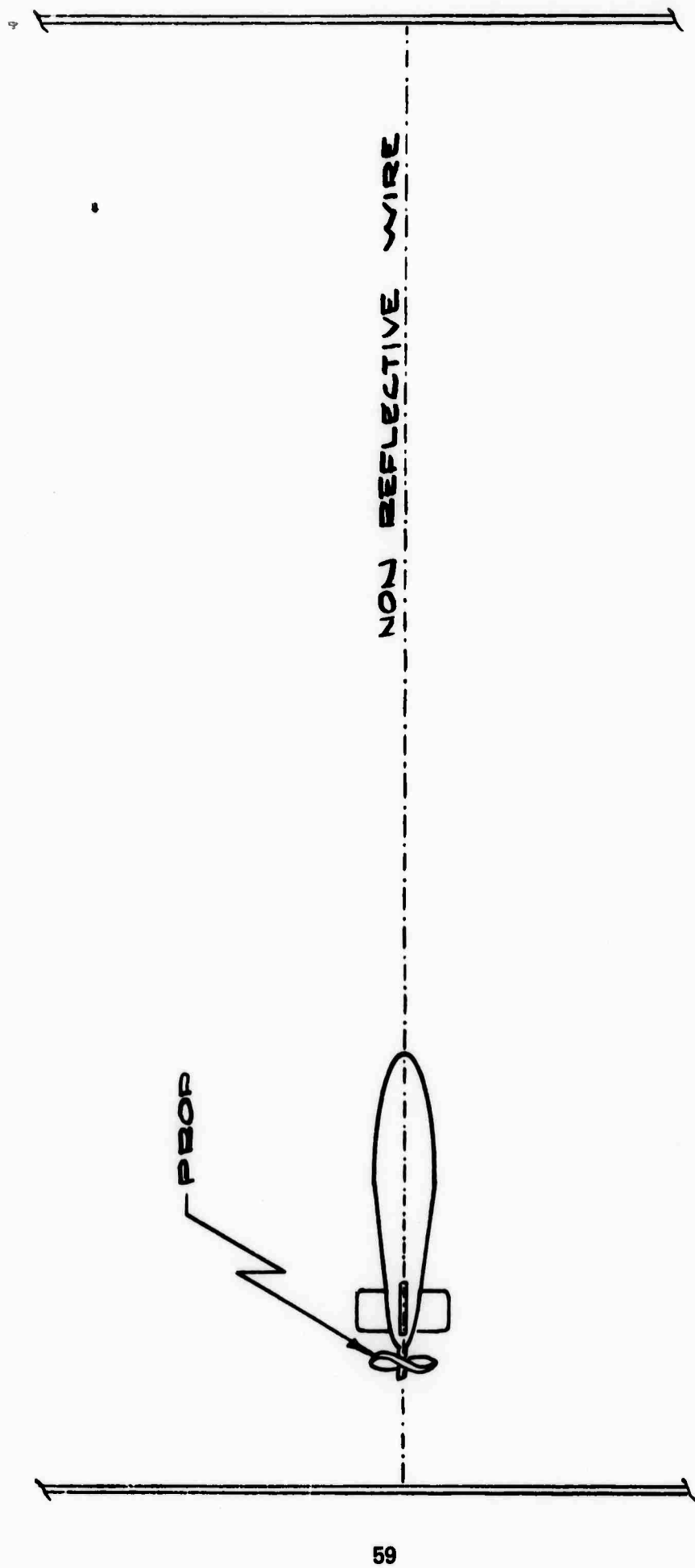
Figure 22. Momentumless Vehicle, Wire Riding (Internal Battery Power).
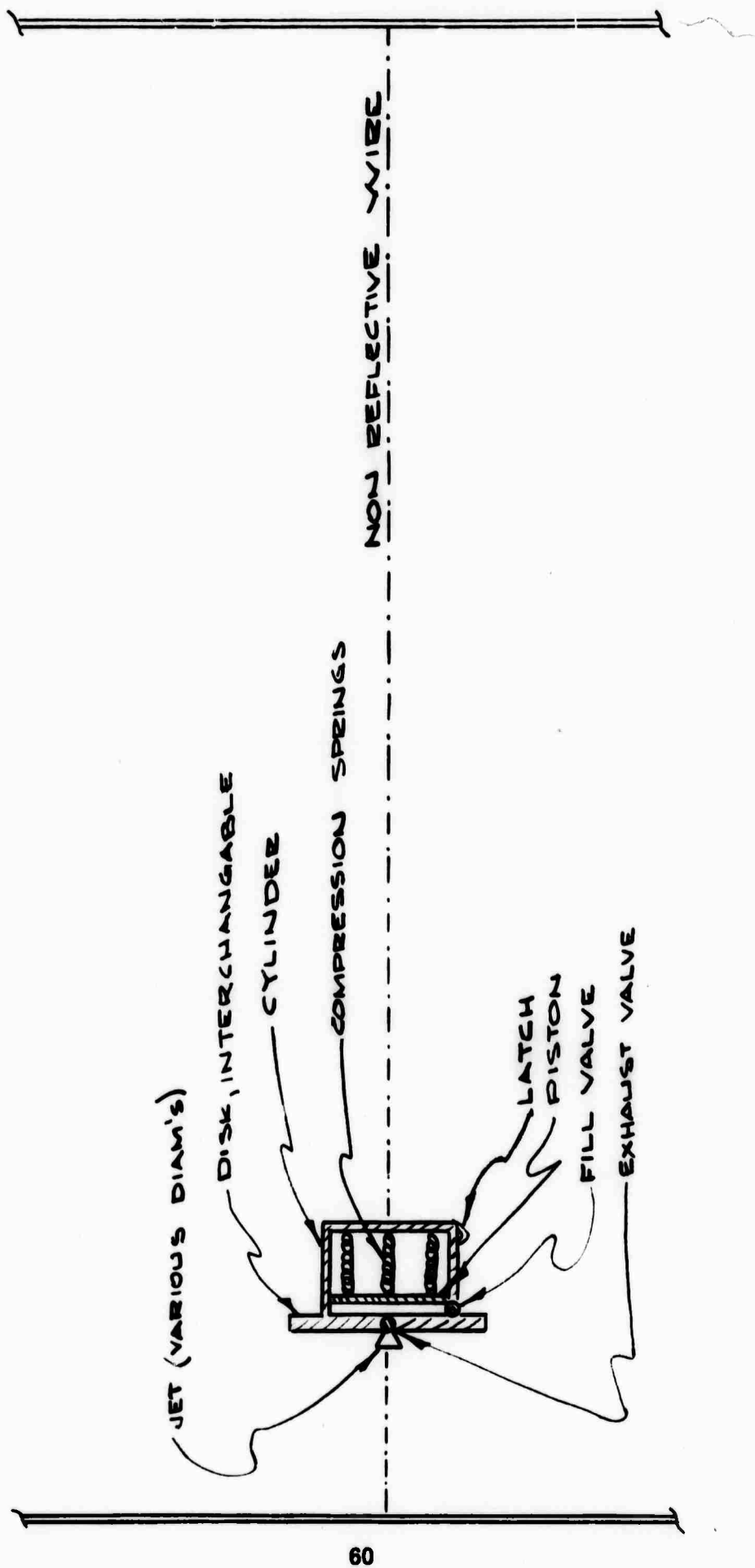
Figure 23. Momentumless Vehicle, Wire Riding (Jet and Disk, Spring Powered).

from the laser, thus allowing operation when other lights are on. The diode quad consists of four photosensitive silicon diodes on a common substrate arranged in four ninety degree pie-shaped sections separated physically and electrically by a gap of 5 mils. The photodiode spectral response peaks in the far red thus matching the laser output. In the control electronics, the four outputs from the diode quad go through buffers and sum and difference networks into control amplifiers to drive the trim tabs. The trim tabs reposition the model so that the laser beam is exactly centered on the diode quad, thus keeping the model on a straight course.

The sketches for the wire riding vehicles are, hopefully, self-explanatory.

APPENDIX A

TWO PARTICLE DATA PROCESSING PROGRAMS

The processing philosophy used in coding the software is similar to the philosophy used in the study on the one particle data. The raw data tapes are cleared of parity errors and converted from 800 to 556 bits per inch to ease the tape reading difficulties. The converted data tapes are reduced into usable particle tracks in a complete program called REDUCE. The reduced tape consists of several tape labels plus a tow label and a data array for each tow containing two particles. The particle data consists of an array containing the cartesian (axial, vertical, and horizontal) coordinate data for both in the particle tank reference system at a particular scan plus the time of the scan for all scans where both tracks were observed. The reduced tape is used as an input to a statistical code which forms the separation vector and samples the time history of this vector at certain times and forms the ensemble sums of various statistical components which are combined into statistical functions used to describe the vector's properties. The output portion of the package converts the ensemble sums into ensemble averages and calculates various statistical functions from the ensembled average statistical components.

The flow diagram of the reduced package is shown in Figure A-1. All portions enclosed within the dashed lines were coded during the current study. The other portions of the code were coded in the one-particle study and are identical to the previous code. In the previous code the angular track responses which make up the tracked particles were checked for TST during each scan and when TST exceeded a certain value the particle track was closed. With the confusion of several responses in each coordinate plus the low values of TST associated with the frequently occurring ghosts the previous method of selecting which tracks form the particles was abandoned as being too expensive and frequently not accurate.

At every scan the current code updates the separate angular tracks which are being observed in each coordinate. The current angular position of the track is saved in a buffer. As the buffer of angular track data is filled it is dumped to a random access disk file for processing at the end of the tow. At the end of the tow the angular tracks are examined to find the range of scans which contain at least two active tracks in each coordinate. If the tow doesn't contain any scans which contain at least two responses in each coordinate
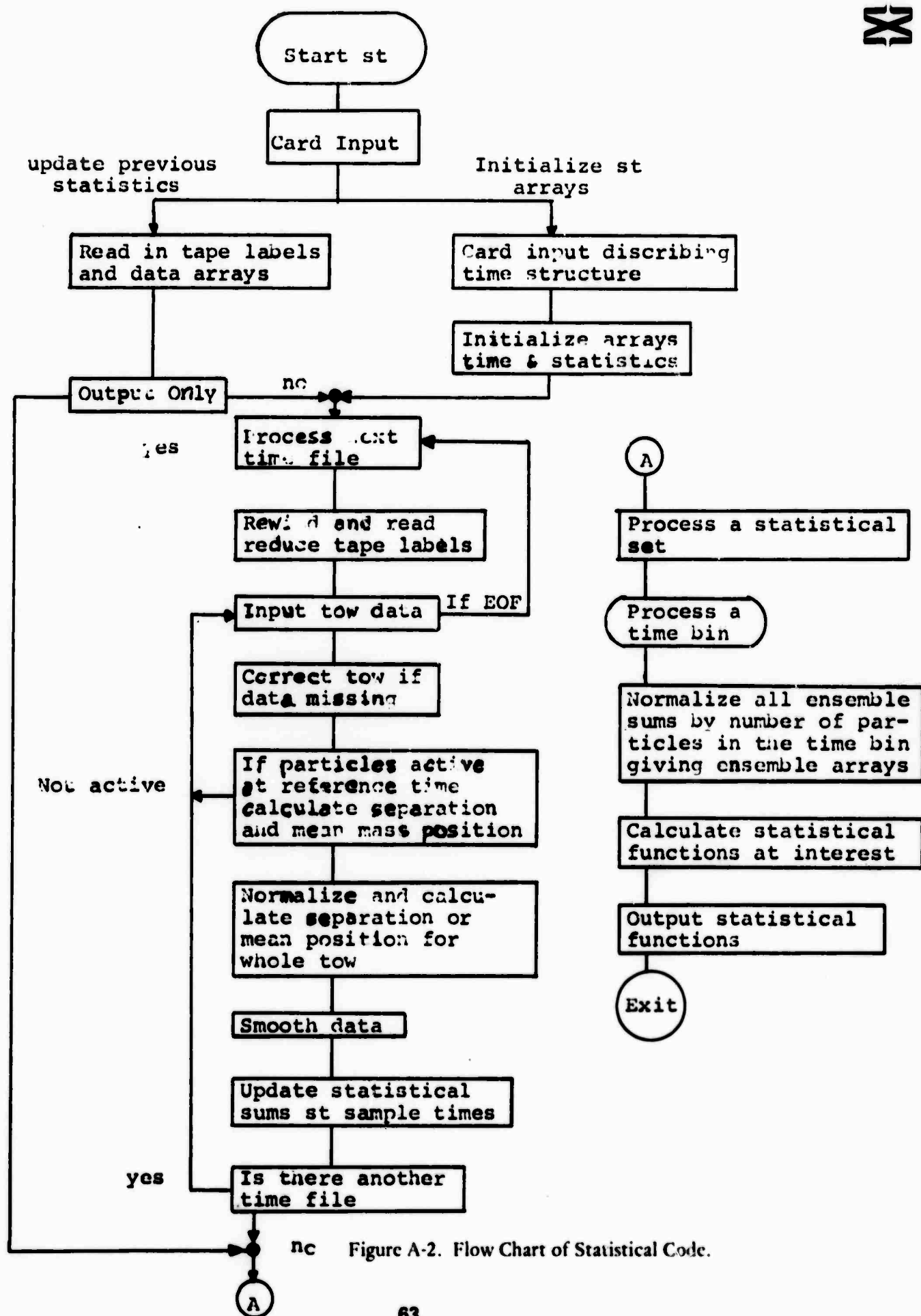
62

Figure A-2. Flow Chart of Statistical Code.

63

the tow is discarded. Three scans are chosen near the beginning, middle, and end of the active scan. At each of these scans the angular track responses in the various coordinates are tested to indicate which combination of responses actually originated from the two particles. The first and second responses in the axial coordinate are arbitrarily defined as belonging to the primary and complimentary particles respectively. All possible combinations of the two possible responses in each coordinate are used to calculate a value of TST from the routine QTST for the set of responses used. In QTST the intersection of the plane defined by the angular responses in the axial, vertical, and horizontal coordinates is used to define the position of the particle which had those coordinate responses. TST is then calculated as the shortest distance between the 'w' plane defined by angular response in 'w' coordinate and the intersection of the three planes. After TST is calculated for all combinations of responses, the responses are separated into all possible primary-complimentary (p-c) combinations and the sum of the squares of both TST's are added. The p-c combination with the lowest sum of squares of TST is selected to be the most likely candidate to have originated from the original particles at that scan. This procedure of selecting a possible p-c set of responses for the particular scan is repeated for the other two scans selected. The p-c combination selected most often in each coordinate will be the final set of responses selected for the tow. Using the selected p-c set of responses the axial, vertical, and horizontal coordinates for each particle are calculated at each active scan and outputted to the reduced tape.

The statistical program is similar to the statistical program in the previous study with several exceptions. First all the different file structures are maintained on one data array and that data is maintained within the core during the operation of the program. The three previous separate programs making up the statistical package (utilization, statistics, and output) have been combined into one package. In addition, the separation vector is not rotated about the axial axis as was necessary in the single particle study. These changes were incorporated to reduce the cost of running the program and became possible by the reduction in the size of the main statistical array. A flow chart of the statistical package is shown in Figure A-2. Initially the statistical arrays are set up by either initializing the arrays for the initial data update or by reading into core from a magnetic tape the data from a previous update. The statistics were maintained on twelve separate data sets within one complete operation of the program on all of the reduced data
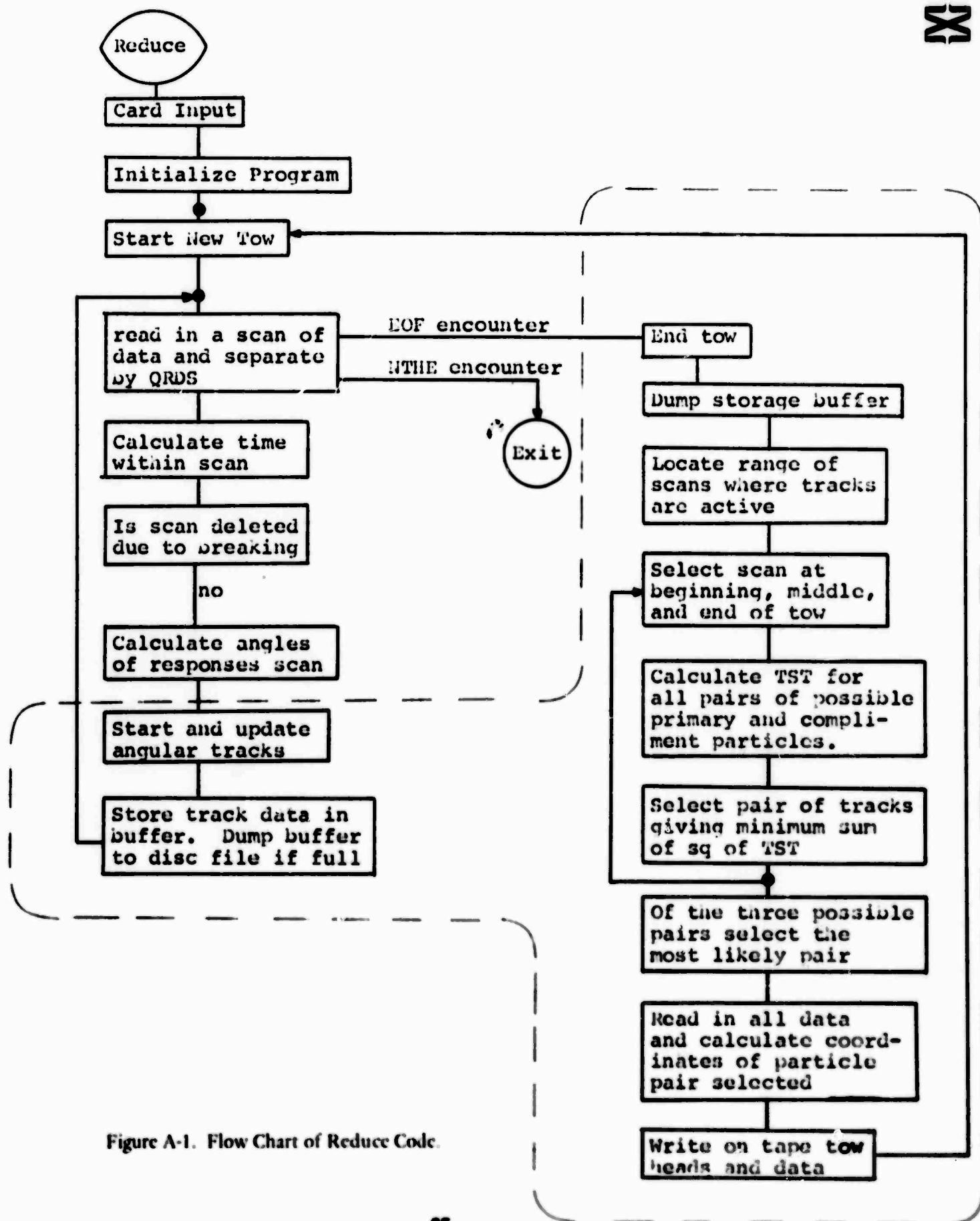
Figure A-1. Flow Chart of Reduce Code.

tapes. These twleve were separated into three time structures plus four separation struc-
tures. Each reduced tape was rewound and processed three times for each of the three
time data sets. During each pass of the tape the particle separation at the initial time
sample of the time data set was calculated and used to determine to which separation
data set the tow belonged.

The separation vector is then calculated and smoothed. Given the smoothed separ-
ation vector the ensemble sums of the statistic components are updated for the particular
sample time and the separation data set. After all of the time sets have been updated all
of the data is outputed.

APPENDIX B

WATER TANK SCANNING SYSTEM

Figure B-1 shows several views of the scanning system. An optical system consisting of mirrors and a high-quality camera lens project an image of particles in the water tank onto the inside surface of a rotating drum. The drum carries several identical groups of three slits; with each of the three slits oriented as shown in Figure B-1. As a slit is carried across the image field by the rotating drum, the apparent slit motion is perpendicular to the orientation of the slit, with the result that the field is scanned in a horizontal direction by the first slit, in a direction 60° below the horizontal by the second slit, and in a direction 60° above the horizontal by the third slit.

As a slit crosses a particle image, the light allowed through the slit is detected by a photomultiplier, the output signal of which actuates some logic operations in the data recording system. After processing by a computer, the data obtained from one of the photomultipliers represents the particle locations as projected on a plane perpendicular to the viewing direction. This information has the form of values for each of three co-planar, non-orthogonal coordinates. Although only two coordinates are required to define a position in a plane, the redundant third coordinate helps resolve the confusion resulting when several coordinate values must be assigned to several different particles.

Two lens-mirror-photomultiplier imaging systems are shown in Figure B-1 combined with one rotating drum. Any reasonable number of imaging systems may be used with a single drum, provided of course that the drum is large enough to accommodate them. The slit groups are arranged around the drum so as to permit the sequences of data pulses from the photomultiplier to be fed into a single data recording input channel without overlapping or large gaps. Control pulses, which mark the beginning of the measurement period for each imaging system, are provided by the photodiodes which intercept light passed by a control slit carried by the drum.

One proposed viewing configuration for the scanner is shown in Figure B-2. With this arrangement particles floating on the surface can be viewed simultaneously with particles at some distance below the surface. The upward-looking imaging system can see all the particles, whereas the side-looking imaging system observes only the submerged particles and supplies height information not provided by the upward-looking system and
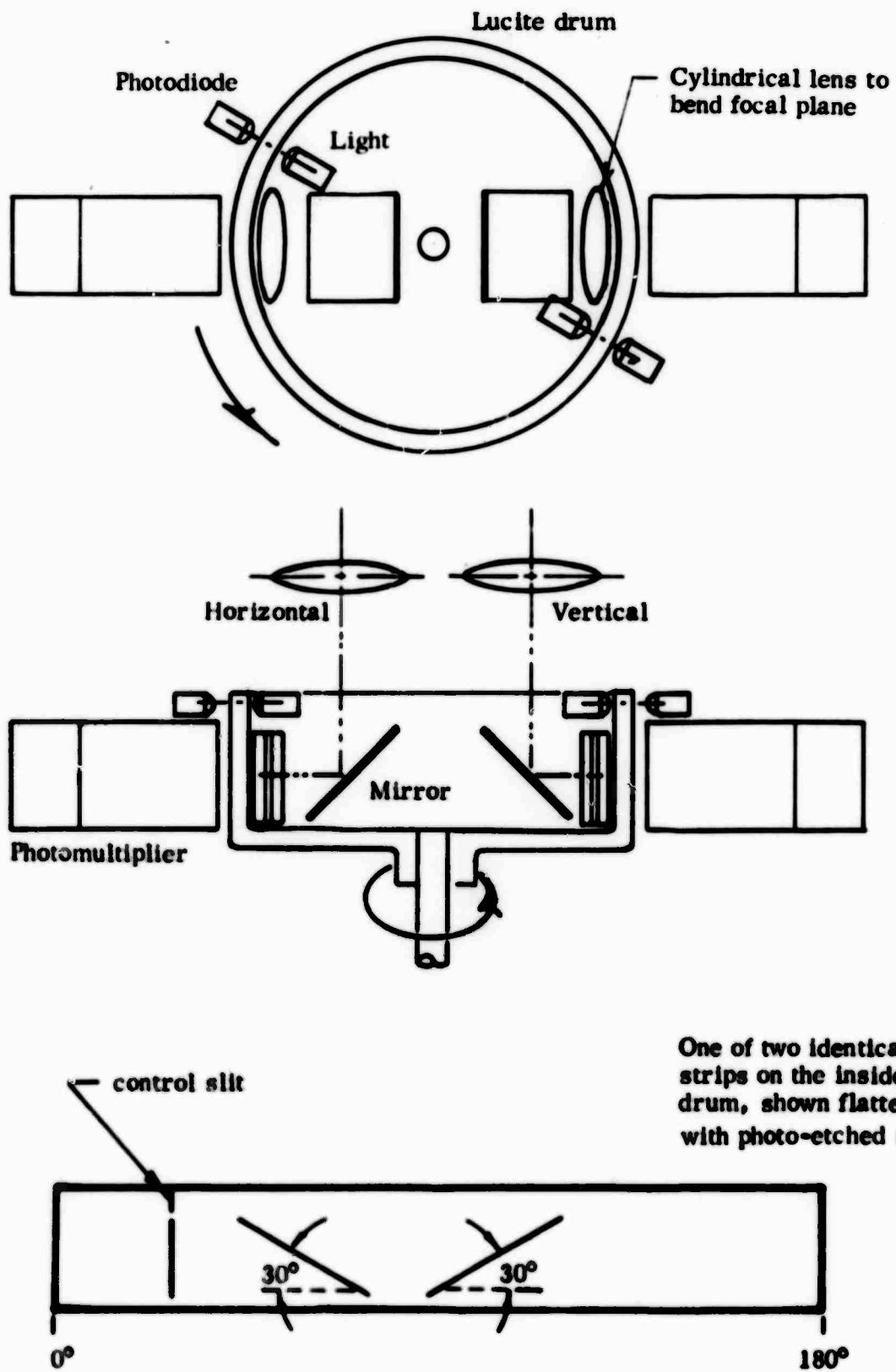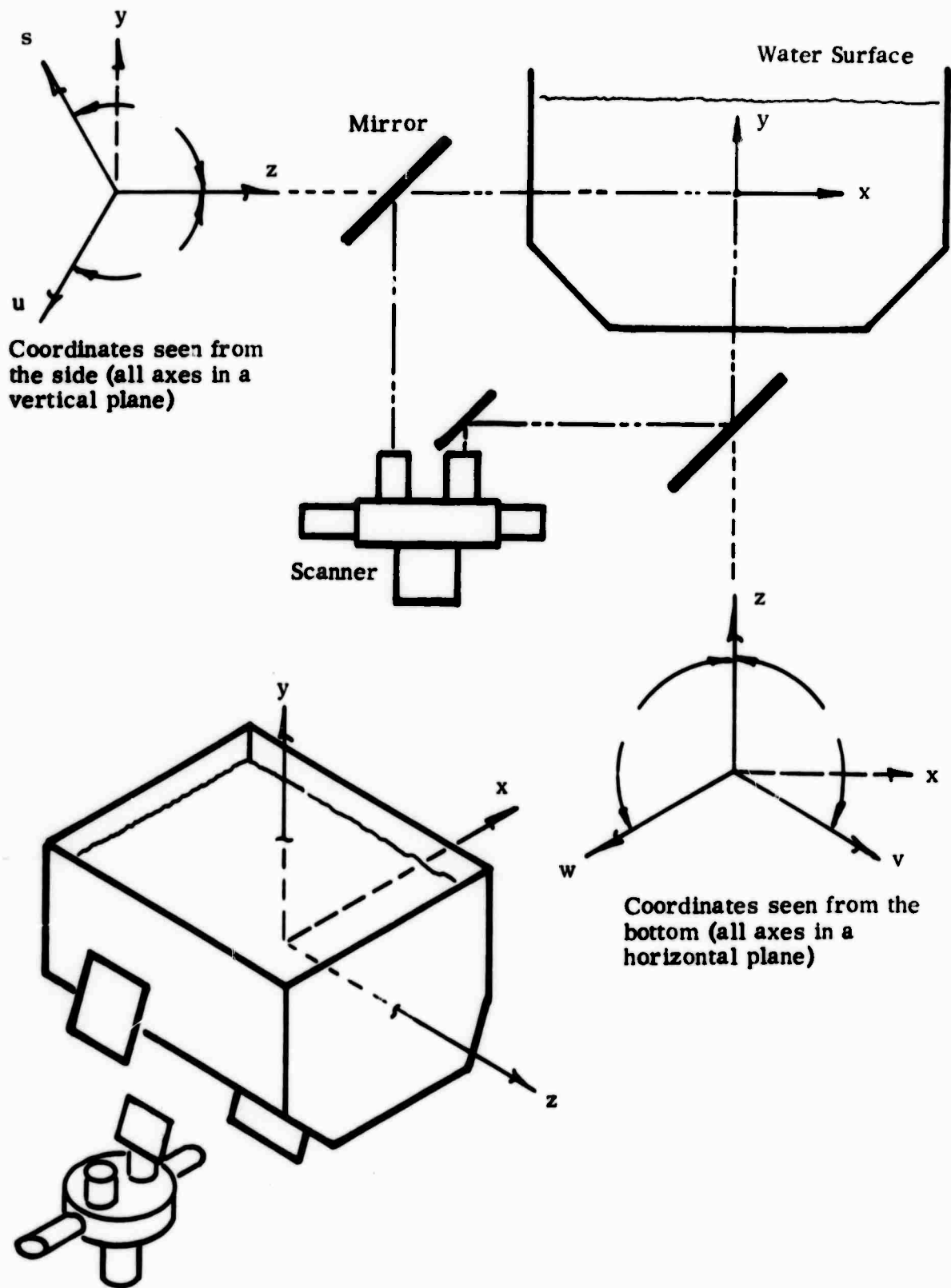
Figure B-1. Scanning System.

Figure B-2. Scanner Viewing Configuration.

not needed for the floating particles. Other configurations are being considered, including one in which the floating particles are viewed from the top. Because of distortions from small waves, the submerged particles cannot also be observed from the top, and if it is desired to observe both submerged and floating particles simultaneously using top viewing for the floating particles, it will be necessary to employ filters or some other means of rendering the lower particles invisible to the top-viewing optical system.

Figure B-3 shows the form taken by the raw data coming from the scanner. The control pulses from the photodiodes are converted into control numbers and are stored in the multichannel scaler memory. In addition, the control pulses cause the scaler to advance to the next counting channel. Pulses representing particles seen by the photomultipliers also cause channel advance events. During the period between pulses the output of an oscillator is counted by the scaler and the counts for the sequence of periods are stored in a corresponding sequence of memory channels. When one segment of the scaler memory is filled, the input is shifted to another segment of the memory while the first segment is read out on magnetic tape. The data on the tape are just a sequence of numbers. The control numbers will be 0 and 1 and the other numbers, which are oscillator output counts and are proportional to the time between pulses, all have 10 added to them before storage so that it is impossible to confuse them with the control numbers.

Processing the data will include the following operations:

1. Distinguishing the control numbers.
2. Subtracting 10 from each of the count numbers.
3. Categorizing the count numbers according to coordinate axis.
4. Converting the count numbers into rough coordinate values (without adjusting for perspective).
5. Sorting the coordinate values according to particle.
6. Adjusting the coordinate values for perspective.

Operation 1 is accomplished by testing whether the data number is less than 10.

Operation 2 is a simple arithmetic operation.

Operation 3 is accomplished by making use of knowledge of the manner in which the time period between control pulses is apportioned among the three coordinates.

Figure B-3. Raw Data From the Scanner.

Control pulse for upward-looking imaging system.

Control pulse for side-looking imaging system

Summed photomultiplier pulses

Recorded intervals
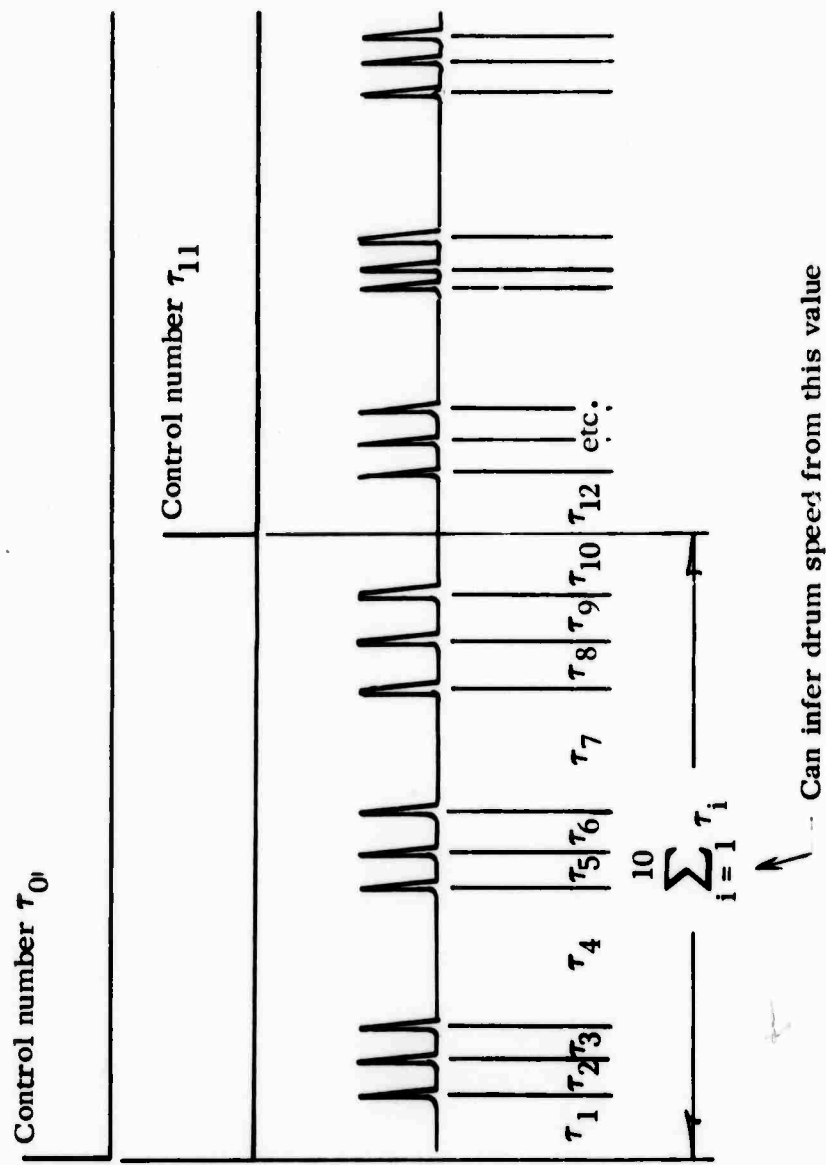
Control number τ_{0}

Control number τ_{11}

τ_1 τ_2 τ_3 τ_4 τ_5 τ_6 τ_7 τ_8 τ_9 τ_{10} τ_{12} etc.

$$\sum_{i=1}^{10} \tau_i$$

Can infer drum speed from this value

71

The coordinate values of Operation 4 are obtained from the sequences of count numbers using expressions of the form

$$z_i = K_z \sum_{j=m}^{n} r_j \cdot C_z ,$$

$$v_i = K_v \sum_{j=m}^{n'} r_j \cdot C_v , \text{ etc.}$$

The sums represent time durations between a control pulse and a pulse produced by a particle image. The constants K and C are determined by using the scanner to observe particles with known positions, or the constants may be calculated from known parameters. The constants C depend on the distance between the control slit and the slit associated with the coordinate in question. The constants K depend on the drum speed and on the angle of inclination of the slit. Because of the problem of perspective, the quantities z, v, w, etc. actually represent angles subtended at the lens by the observed particle and the optic axis of the viewing system. These quantities can be converted to projections on a coordinate plane after Operation 5.

Before Operation 5 is performed all we have is a list of z values, v values, w values, etc., but we do not know which v value and w value go together with a particular z value to represent a particle position. The redundant coordinates aid in solving this problem, since they permit us to apply to each possible combination of values a mathematical test. For three coplanar coordinates 120° apart the test has the very simple form

$$z + v + w \leqslant \epsilon$$

or

$$z' + s + u \leqslant \epsilon$$

where ϵ is a small number related to the measurement accuracy. Unfortunately, when there are a large number of particles it is probable that there will be several combinations which accidentally satisfy the test but do not represent real particles. These 'ghosts' may be distinguished from genuine particles by using the fact that the existence of the ghosts

72

is transitory as the particles move around, whereas a genuine particle should persist in time. The persistence requirement is equivalent to requiring continuity of the particle path. Thus, a continuity test of the form

$$z(t + \Delta t) - z(t) < \epsilon$$

$$v(t + \Delta t) - v(t) < \epsilon$$

is applied to the combinations of coordinate values. Successive combinations of coordinate values which satisfy both the redundant coordinate test and the continuity test for an extended period of time are considered to represent a particle.

For the viewing configuration shown in Figure B-2 the particles floating on top can be identified by the fact that they have no side-looking coordinates, that is, for a sequence of z, v, and w values which have passed the redundant coordinate and continuity tests there is no sequence of z', s, and u values which have also passed the tests and for which $z' - z < \epsilon$. A sequence of z, v, w, z', u, and s values which have passed the redundant coordinate tests $z + v + w < \epsilon$ and $|z' + u + s| < \epsilon$, which have passed the continuity tests, and for which $|z' - z| < \epsilon$ for an extended period of time will be considered to represent a single submerged particle.

Just before applying the test $|z' - z| < \epsilon$ it is necessary to adjust the z' and z values for perspective. The computer time for the tests to sort out the coordinate values can be appreciably reduced, without any loss of accuracy, if all the sorting operations except the $|z' - z| < \epsilon$ test are completed prior to adjusting the coordinate values (Operation 6). Then the adjustments are made on only the final combination of coordinate values which survive the tests and not on all the tentative combinations, each one requiring a different adjustment depending on the tentative coordinate values. The adjustments are not needed for the comparison tests

$$|z + v + w| < \epsilon$$

$$|z' + s + u| < \epsilon$$

73

because the coordinates involved in each test lie in a plane perpendicular to the viewing direction and the coordinate values all scale up and down together as the distance to the lens is varied.

The scanning system described above represents an improvement on the system previously used to track particles. The new system uses fewer lenses and photomultipliers but produces data with greater redundancy, making it possible to simultaneously track more particles than previously. The use of just one lens per viewing direction simplifies setting up and focusing and minimizes the complexity of the required data processing.

Fortunately, the old scanner housing, motor, and photomultipliers may be used for the new system, and the previous data recording system may be used with just one minor modification to reduce the number of control numbers from 4 to 2. The conditions for the contemplated experiments are less severe than conditions for previous successful tracking experiments, since slower scanning rates are now permitted. Thus, we expect to have no trouble obtaining adequate signal-to-noise ratios.

REFERENCES

1. *Final Technical Summary Report, Contract DAAH01-69-C-1650, The KMS Technology Center (January 1971).*

2. *Richardson, L.F., Proc. Roy. Soc. A, 110, 709 (1926).*

3. *Townsend, A.A., The Structure of Turbulent Shear Flow, Cambridge University Press, Cambridge (1956).*

4. *Gibson, C.H., Chen, C.C. and Lin, S.C., AIAA J., 6, 642 (1968).*